Evaluation of the flame propagation within a SI engine using flame imaging and LES

Combustion Theory and Modelling
Vol. 00, No. 00, Month 200x, 1–60

RESEARCH ARTICLE

Evaluation of the flame propagation within a SI engine using flame imaging and LES

Chao He[a,b*], Guido Kuenne[a], Esra Yildar[a], Jeroen van Oijen[e], Francesca di Mare[c], Amsini Sadiki[a], Carl-Philipp Ding[c], Elias Baum[c], Brian Peterson[d], Benjamin Böhm[a] and Johannes Janicka[a]

[a]*Institute of Energy and Power Plant Technology, TU Darmstadt, Jovanka-Bontschits-Strasse 2, 64287 Darmstadt, Germany*; [b]*Graduate School of Computational Engineering, TU Darmstadt, Dolivostrasse 15, 64293 Darmstadt, Germany*; [c]*Institute Reactive Flows and Diagnostics, TU Darmstadt, Jovanka-Bontschits-Strasse 2, 64287 Darmstadt, Germany*; [d] *Institute of Multiscale Thermofluids, School of Engineering, The University of Edinburgh, King's Buildings, Mayfield Road, Edinburgh, EH9 3DW, UK*; [e]*Multiphase & Reactive Flows, Department of Mechanical Engineering, Eindhoven University of Technology, P.O. Box 513, 5600 MB Eindhoven, The Netherlands*

(*Received 00 Month 200x; final version received 00 Month 200x*)

This work shows experiments and simulations of the fired operation of a spark ignition engine with port-fueled injection. The test-rig considered is an optically accessible single cylinder engine specifically designed at TU Darmstadt for the detailed investigation of in-cylinder processes and model validation. The engine was operated under lean conditions using iso-octane as a substitute for gasoline. Experiments have been conducted to provide a sound database of the combustion process. A planar flame imaging technique has been applied within the swirl and tumble plane to provide statistical information on the combustion process to complement the pressure-based comparison between simulation and experiments. This data is then analyzed and used to assess the Large Eddy Simulation performed within this work. For the simulation, the engine code KIVA has been extended by the dynamically thickened flame model combined with chemistry reduction by means of pressure dependent tabulation. 60 cycles have been simulated to perform a statistical evaluation. Based on a detailed comparison with the experimental data, a systematic study has been conducted to obtain insight into the most crucial modeling uncertainties.

Keywords: internal combustion engine; spark ignition; tabulated chemistry; thickened flame; flame imaging

1. Introduction

The internal combustion engine (ICE) has been recognized as one of the most influential inventions by humankind that ever had a greater impact on society, the economy, and the environment [1]. In order to reduce the depletion of petroleum-based fossil fuels and anthropogenic climate change, automotive researchers and manufacturers are now more than ever striving to develop cleaner, more efficient ICEs. This starts with the development of cleaner combustion technology. The development focuses on geometrical improvements (e.g. downsizing) or the

*Corresponding author. Email: he@ekt.tu-darmstadt.de

ISSN: 1364-7830 print/ISSN 1741-3559 online

DOI: 10.1080/13647830.YYYY.xxxxxx
http://www.tandfonline.com

use of 'advanced modes of combustion' (e.g. lean combustion, HCCI, charge stratification, and direct-injection), which can offer 10-40 % improvement in fuel efficiency and CO_2 reduction compared to conventional operation [2–6]. Successful implementation of new ICE technology first requires a very fundamental understanding of the physical processes responsible for fuel-energy conversion and pollutant formation under engine relevant conditions.

Advanced, non-intrusive diagnostic methods and high-fidelity numerical simulations are at the forefront of understanding the fundamental science that aids in the development of cleaner combustion technology [7–12]. As many of the processes in ICEs involve a highly transient turbulent flow field, numerical simulations often utilize simplifying assumptions and models, such that the simulations can be less predictive. Thus, guidance from advanced laser diagnostic methods are used to validate and develop more predictive simulations. Specifically designed engine test-rigs are important to provide a comprehensive experimental database that can be used to study fundamentals of flows, sprays, and combustion.

In the literature, there exist several well documented experimental engine test-rigs. In this regard many of the studies arose from the Sandia Diesel engine [13, 14], the GM R&D test-rig [3, 15, 16], the TCC-III engine in Michigan [17, 18], the SGEmac (IFP) engine [19], and the Darmstadt test-rig [20–22]. The corresponding databases have provided a stronghold for engine simulations with regards to model validation and development. Together, experimental and (RANS-) modeling studies have jointly addressed studies of flow cycle-to-cycle variations (ccv) [14, 23], sprays [15], ignition [24–26], and combustion [27]. Large Eddy Simulation (LES) studies have primarily been concentrated with the SGEmac, Darmstadt, and TCC-III engine databases. Of these studies they have extensively studied the non-reacting flow physics pertaining to ccv [18, 28].

LES has also been applied to the reacting flow of internal combustion engines [29]. Within Spark Ignition (SI) engines (as considered in this work), the model needs to capture the turbulent flame propagation that can be partially resolved within the LES. Accordingly, the majority of SI engine simulations employ LES combustion models that have already been established in this regard within other applications. Specifically, numerous works use the Flame Surface Density (FSD) approach [30, 31], the G-equation [32], the Artificially Thickened Flame (ATF) model [33] and also a few applications based on Probability Density Functions (PDF) [34, 35] exist.

These LES works of SI engines have been initiated by Richard et al. [30] who applied different combustion models to a single cycle. Within later works Enaux et al. [36] simulated 25 consecutive cycles to study ccv. The computational domain included a significant part of the intake and exhaust geometry to allow for appropriate boundary conditions. Very recent studies used LES for a more in-depth analysis for ccv [31]. Besides ccv, near wall combustion [37] and engine knock [38–40] belong to the phenomena simulated within SI engines. Within these works chemistry is treated by reduced mechanisms. In order to account for detailed chemistry effects, also tabulation has already been applied to diesel engines [41, 42], spark assisted HCCI-engines [27], and to treat the auto ignition of engine knock [40]. Regarding the configuration, most of these studies considered the single-cylinder optical SGEmac engine [19] operating with a propane-air mixture where the pressure curves were used as the assessment criteria.

The numerous works using LES in ICE showed the capabilities of the method. Compared to the RANS approach it reduces the modeled part of the solution and therewith the corresponding uncertainties. Furthermore, the availability of transient, spatially resolved data enables important insights into the process. With that, the LES is potentially a very powerful tool within the engine design process as well as for fundamental research. However, deficiencies have also been revealed indicating that the models still suffer weaknesses that can lead to predictions of the simulations that deviate from experimental data. This is caused by the complex physical processes that become increasingly difficult under engine conditions. In this regard the modeling of the turbulent flame kernel expansion determined by intense, only partially resolvable wrinkling under high pressure is of primary importance. Accordingly, findings about the modeling uncertainties using detailed experimental data are desirable. At this, Granet et al. [43] performed a first qualitative comparison of measured and simulated flame kernel shapes which enables a more distinct model evaluation compared to the pressure curve that provides an integral assessment criterion only.

In this work, we look at the flame propagation in a spark-ignition engine operating with an iso-octane/air mixture. Port-fueled injection is used to obtain homogeneous lean conditions as this mode potentially offers increased thermal efficiencies and reduced pollutant emissions when compared to higher equivalence ratios [44]. Furthermore, this setup provided well suited conditions for the optical measurements. The engine simulated is the engine test-rig at TU Darmstadt, which is specially designed to investigate in-cylinder processes and provide valuable data for model validation [20]. LES was already applied to the motored operation [45, 46] and Nguyen et al. [47] showed results from individual cycles of the fired mode. The objectives of this work are:

- Provide an experimental database well designed to characterize the combustion process and for model validation.
- Demonstrate the application of tabulated chemistry combined with the Dynamically Thickened Flame Model (DTFM) to the flame propagation within a SI engine.
- Perform a statistical comparison of experiments and LES for the fired operation of this test-rig.
- Investigate the sensitivity of the results with respect to the most significant modeling uncertainties.
- Besides the pressure curves we utilize flame imaging as a second quantitative assessment parameter being directly linked to the prediction of the flame kernel expansion.

2. Configuration and experimental characterization

The configuration considered is an optically accessible single-cylinder direct-injection spark-ignition engine (AVL). The engine is equipped with a four-valve pent-roof cylinder head, a side-mounted injector, centrally-mounted spark plug, a quartz-glass liner and flat piston window. The optical engine is embedded in a test-rig facility specifically designed to provide reproducible engine operating conditions and well controlled boundary conditions. For this work, the side-mounted injector remained inactive, while iso-octane fuel was injected via a port-fuel

injection located approx. 1 m upstream the engine to ensure homogeneous fuel-air mixtures.

[Table 1 about here.]

Figure 1 shows the cylinder head with part of the intake and exhaust manifold. The locations of the temperature and pressure sensors in the intake and exhaust manifold are indicated and correspond to the extent of the computational domain. A detailed description of the test facility, engine geometry, boundary conditions and experimental measurements of the motored in-cylinder flow can be found in [20, 21, 48]. In this work the boundary conditions of the fired operation are shown. Operating conditions are given in Table 1.

[Figure 1 about here.]

Spark timing was set to achieve stable operation for the given equivalence ratio (ϕ=0.8). The dwell time was 3.5 ms and the mean spark duration was 0.8 ms. The temperatures in the intake and exhaust manifold were measured using PT-100 thermocouples. The pressure was recorded using piezoelectric pressure sensors (AVL) with a measurement uncertainty of 0.5 %. Figure 2 shows the pressure of the cylinder, intake and exhaust manifold of all 600 processed cycles. The in-cylinder pressure shows that the operating point is very stable. Before ignition timing the standard deviation of the in-cylinder pressure is very low. After ignition the in-cylinder pressure deviates between cycles due to cycle-to-cycle fluctuations. The standard deviation of the in-cylinder pressure is about 2 bar and there are no cycles that strongly deviate from the mean trace (e.g. misfires).

The intake manifold pressure shows a similar behavior to the motored case with standard deviations much less than 1 % confirming the repeatability of the boundary conditions during operation. The exhaust manifold pressure trace has a higher standard deviation. There are two main reasons for this; first, the cycle-to-cycle deviations of the in-cylinder pressure lead to fluctuations in the exhaust manifold as soon as the exhaust valves open (valve lift is also indicated in Fig. 2). Second, the exhaust manifold heats up during fired operation which causes the exhaust gas temperature to rise during the recordings leading to a change in frequency at which the pressure in the exhaust manifold oscillates.

[Figure 2 about here.]

To determine the enflamed region, the intake flow was seeded with silicone oil-droplets (Dow Corning 510 cSt-50) using an aerosol generator (Palas 10.0). The estimated droplet size was 0.5 μm. The oil-droplets that evaporate in the flame are a sufficiently accurate marker to identify burned gas regions within the engine [49]. The effect of the seeded oil-droplets on the combustion performance was evaluated and it was found, that the silicone oil has no significant influence (Fig. 3). This is corroborated by the fact that seeded oil-droplet densities are not enough to sustain a flame kernel [50].

[Figure 3 about here.]

Figure 4 shows a schematic of the experimental setup used for flame imaging.

Measurements were acquired in the central tumble plane (y=0 mm) and a horizontal (swirl) plane 1.4 mm below the spark plug. For each plane the setup was changed accordingly. The spatial extents of the acquired images are limited by the field-of-view, being 38x12 mm^2 (34.5 pxl/mm) in the tumble plane and 43x70 mm^2 (18.5 pxl/mm) in the swirl plane. Droplets were illuminated using a frequency doubled Nd:YAG high-speed laser (Edgewave, INNOSLAB, 532 nm), operated at 2.4 KHz, and scattered light was detected using a CMOS camera (LaVision, Phantom v711) equipped with 50 mm lenses (Nikon, f/1.2). Flame luminosity was suppressed using a bandpass filter centered at 532 nm. Laser and camera were synchronized to the crank shaft encoder with a high-speed controller (LaVision, HSCv2). The laser light sheet was expanded and collimated using two cylindrical lenses with f=-50 mm and f=750 mm and then focused using a cylindrical lens with f=1000 mm. Laser sheet thickness was 0.6 mm ($1/e^2$).

[Figure 4 about here.]

Measurements in the tumble plane and swirl plane were performed separately. Three runs were recorded for each plane, with two hundred fired cycles per run. The last hundred cycles of each run were used to calculate flame statistics. Accordingly, flame statistics consist of 300 cycles for each plane. Images were acquired every second crank angle degree (cad; negative values represent cad before compression top dead center) starting at ignition at -16 cad until 2 cad. Figure 5 shows raw-images for an individual ignition event. After background subtraction and normalization, the images were filtered using a local median filter (21 pixel). The images were then binarized using an adaptive threshold method to identify burnt and unburnt regions similar to the processing in [51]. From the binarized images the relative frequency of occurrence of the flame was determined for every recorded cad.

[Figure 5 about here.]

3. Numerical modeling

Simulations were conducted with the KIVA-4mpi code [52, 53]. For this work it has been extended to compute the combustion process with the DTFM [54] in combination with FGM tabulated chemistry [55, 56] as detailed in Section 3.2. Within this framework the system gets closed using the equation of state

$$p = \rho \frac{\mathcal{R}}{\mathcal{M}} T \tag{1}$$

and the transport equations for continuity, momentum, enthalpy and the reaction progress variable

$$\frac{\partial \overline{\rho}}{\partial t} + \frac{\partial (\overline{\rho} \widetilde{u}_j)}{\partial x_j} = 0 \tag{2}$$

$$\frac{\partial (\overline{\rho} \widetilde{u}_i)}{\partial t} + \frac{\partial (\overline{\rho} \widetilde{u}_i \widetilde{u}_j)}{\partial x_j} = -\frac{\partial \overline{P}}{\partial x_i} + \frac{\partial}{\partial x_j} \left[(\bar{\mu} + \mu_t) \left(\frac{\partial \widetilde{u}_i}{\partial x_j} + \frac{\partial \widetilde{u}_j}{\partial x_i} - \frac{2}{3} \frac{\partial \widetilde{u}_k}{\partial x_k} \delta_{ij} \right) \right] + \overline{\rho} g_i \tag{3}$$

$$\frac{\partial(\overline{\rho}\widetilde{h})}{\partial t}+\frac{\partial(\overline{\rho}\widetilde{h}\,\widetilde{u}_j)}{\partial x_j}=\frac{\partial\overline{p}}{\partial t}+\widetilde{\tau}_{ij}\frac{\partial\widetilde{u}_i}{\partial x_j}+\frac{\partial}{\partial x_j}\left[\frac{\mathcal{F}\mathcal{E}\overline{\mu}+(1-\Omega)\,\mu_t}{Pr}\frac{\partial\widetilde{h}}{\partial x_j}\right] \tag{4}$$

$$\frac{\partial(\overline{\rho}\widetilde{Y}_{\mathrm{CO_2}})}{\partial t}+\frac{\partial(\overline{\rho}\widetilde{Y}_{\mathrm{CO_2}}\widetilde{u}_j)}{\partial x_j}=\frac{\partial}{\partial x_j}\left[\frac{\mathcal{F}\mathcal{E}\overline{\mu}+(1-\Omega)\,\mu_t}{Sc}\frac{\partial\widetilde{Y}_{\mathrm{CO_2}}}{\partial x_j}\right]+\frac{\mathcal{E}}{\mathcal{F}}\dot{\omega}_{\mathrm{CO_2}} \tag{5}$$

where $\mathcal{E}$ and $\mathcal{F}$ denote the efficiency function and thickening factor as detailed in Section 3.2, respectively. The code is second order in space and the Smagorinsky model is used for the subgrid closure of momentum. It uses the Arbitrary Lagrangian-Eulerian (ALE) scheme to follow the moving geometry.

3.1 *Computational domain*

As indicated in Fig. 1, the temperature and pressure of the intake and exhaust flow are measured 10 pipe diameters (D) upstream and 7D downstream of the combustion chamber. Accordingly, the computational domain extends to these positions such that these measurements can be used as boundary conditions (see bottom left of Fig. 7) for the LES. These measured pressures, as applied in the simulation, were introduced in the middle of Fig. 2 as a function of the cad. The pressure traces within the intake and exhaust systems reveal the typical pressure behavior shown for single-cylinder engines, which is caused by the pressure waves created by valve opening and closing. As mentioned in Section 2, the variation of this quantity in between cycles is negligible and we therefore applied the same trace for each cycle within the simulation. Complemented by the temperature provided (not shown), all other quantities evolve naturally in the simulation as a part of the solution. Important in this regard is the mass flux that finally leads to the trapped mass within the cylinder which in turn has a significant impact onto the pressure curve. Since there are many potential sources for errors (e.g. grid, geometric approximations, and valve lift) we first used the motored case as a basic assessment of the numerical setup. Figure 6 shows the corresponding phase-averaged pressure curve of this motored operation. The 50 cycles averaged in the simulation and experiment are in good agreement which indicates that the overall numerical setup reproduced the correct trapped mass as is important when going to the fired operation.

[Figure 6 about here.]

The grid is illustrated in Fig. 7 and 8. As one can see the geometry is mapped onto boundary-fitted hexahedral cells that follow the moving geometry within the ALE approach. Accordingly, the mesh size varies from approximately 2 million to 4 million cells throughout the cycle at which the timestep-size adjusts according to numerical accuracy and stability requirements ($0.1-1\,\mu$s). During the flame propagation (bottom of Fig. 8) the cell size is about $\Delta_{\mathrm{x}}=0.4\,$mm.

[Figure 7 about here.]

[Figure 8 about here.]

3.2 *Combustion modeling*

3.2.1 Chemistry reduction by tabulation

[Figure 9 about here.]

The chemical reaction is mapped onto controlling variables following the FGM methodology [55, 56]. The pre-computed thermo-chemical states are based on the detailed mechanism of Blanquart et al. [57] describing the reaction of iso-octane by means of 148 species and 928 elementary reactions. According to the premixed combustion mode within the SI engine, freely propagating flames are used. To cover the engine relevant conditions, a series of these flamelets was computed for a range of pressure and enthalpy levels using the one-dimensional code CHEM1D [58]. The resulting three-dimensional lookup-table is illustrated in Fig. 9. Shown here is the variation of the chemical source term within the relevant subsection of the table during flame propagation.

3.2.2 ATF and KIVA coupling

The lookup-table is embedded into the ALE-scheme by providing the viscosity, chemical source term, heat capacity, temperature and molar mass:

$$\mu, \omega_{\mathrm{CO_2}}, c_\mathrm{p}, T, \mathcal{M} = f(p, h, Y_{\mathrm{CO_2}}) \tag{6}$$

for the iterative procedure solving the set of Eq. (1)-(5). By tabulating the chemistry, the mesh resolution required to capture the flame gets reduced to the scales of the transported species being in the order of the thermal layer thickness:

$$\delta = \frac{T_\mathrm{b} - T_\mathrm{u}}{\max\left(\frac{\partial T}{\partial x}\right)}. \tag{7}$$

We intentionally transport the enthalpy itself (Eq. (4)) instead of its sensible form to avoid the heat release leaving the chemical source term of the progress variable (Eq. (5)) as the most stringent scale to be resolved. We observed that the flame speed predicted is sufficiently accurate for the full range of possible states as long as the maximum grid size satisfies:

$$\Delta_{\mathrm{x,max}} \leq \delta/3. \tag{8}$$

The functionality of this coupling between the chemistry table and KIVA is demonstrated in Fig. 10: the top shows the flame speed for the engine relevant range of unburnt gas temperatures (T_u) and pressures (p). One can see, that KIVA reproduces the detailed chemistry solution for this undisturbed freely propagating flame very accurately. The transferability of these results to turbulent flames where strain and curvature alter the propagation speed was demonstrated in [59–61]. The lower plot shows the flame structure for conditions found at about 10 cad after ignition. Here, the spatial evolution of the flame is given by the temperature and the chemical source term of CO_2, representing the large and small scales of the flame to be resolved, respectively. Just as for the flame speeds the results are in good agreement.

[Figure 10 about here.]

[Figure 11 about here.]

Still, as will be illustrated in the next section, the limiting grid size, given by Eq. (8), is exceeded by far for typical grids, especially since the flame thickness reduces throughout the process caused by the rising pressure. This problem encountered in all simulations of realistic devices is treated with the ATF-model in this work entering the governing equations (4) and (5) by the thickening factor $\mathcal{F}$ and the efficiency function $\mathcal{E}$. Their basic functions are illustrated in Fig. 11 where the original flame front (as it would be obtained on a fully resolving grid) is given by the red line. First, the flame structure is made resolvable by artificially thickening it by the factor $\mathcal{F}$ corresponding to a mathematical transformation which preserves the laminar propagation speed. We use the dynamic formulation to limit the thickening to the flame region using the flame sensor Ω according to

$$\mathcal{F} = 1 + (\mathcal{F}_{\max} - 1)\,\Omega \quad \text{with} \tag{9}$$

$$\Omega = 16[c(1-c)]^2 \quad \text{where} \quad c = \frac{\widetilde{Y}_{\mathrm{CO_2}} - Y^{\min}_{\mathrm{CO_2}}}{Y^{\max}_{\mathrm{CO_2}} - Y^{\min}_{\mathrm{CO_2}}}. \tag{10}$$

Herein the maximum thickening factor $\mathcal{F}_{\max}$ adjusts to the grid size, using:

$$\mathcal{F}_{\max} = \frac{\Delta_{\mathrm{x}}}{\Delta_{\mathrm{x,max}}}. \tag{11}$$

Furthermore, for the application within engines this thickening factor must also adjust to the pressure which is realized by adding the flame thickness δ to the variables extracted from the table (see. Eq. (6)). $\mathcal{F}$ then simply follows from Eq. (8)-(11) by using

$$\delta = f(p, h). \tag{12}$$

The flame front found after the thickening procedure is given by the blue line in Fig. 11. Due to the thickening, the flame becomes less sensitive to turbulent wrinkling and accordingly an effective area of fuel consumption is lost when compared to the original flame. This unresolved wrinkling needs to be compensated for by an efficiency function that yields, according to the area ratio of the actual and modeled flame, an increase of the flame speed by

$$\mathcal{E} = \frac{s_{\mathrm{T,LES}}}{s_{\mathrm{L}}}. \tag{13}$$

Accordingly the flame front resolved within the LES will propagate with $s_{\mathrm{T,LES}}$ which results from spatial filtering and is a numerical property not to be confused with the classical turbulent flame speed associated with temporal averaging. Since the area ratio is unknown, the efficiency function can only be estimated which represents the major uncertainty within the ATF approach. Within this work, the efficiency function is estimated according to Charlette et al. [62]

$$\mathcal{E} = f\left(\mathcal{F}, \frac{u'_\Delta}{s_{\mathrm{L}}}\right) = \left[1 + \min\left(\mathcal{F}, \Gamma\frac{u'_\Delta}{s_{\mathrm{L}}}\right)\right]^\beta \tag{14}$$

where u'_Δ represents the turbulence of the subgrid scale [63] and β is the scaling exponent. The expression is plotted in Fig. 12 where one can see that the increased

flame speed according to the estimated lost flame area is easily a multiple of the original one, especially with the large thickening factors required within engines. For this expression additionally the flame speed s_L is stored in the chemistry table analogous to Eq. (12).

[Figure 12 about here.]

3.2.3 Cycle illustration

Figure 13 illustrates how the lookup-table is employed within the actual process. Given here is a slice of the table showing several quantities within the pressure-enthalpy plane. The first quantity, shown in the gray-scale color, is the flame thickness δ. As mentioned, it is used to dynamically determine the necessary thickening factor during the flame kernel expansion and varies significantly with pressure and enthalpy. As a second quantity, the flame speed has been added by white iso-lines. As is known, it reduces with the pressure but increases with the enthalpy level.

Finally, the circles show some states perceived by the flame during combustion for the specific engine operation. They represent data taken from the simulation during a representative cycle. To illustrate the states perceived by the flame only data within the flame front (c=0.1 to c=0.9) has been gathered. One can see, that for each cad, the pressure is very constant while a certain scatter in the enthalpy is found at different spatial locations. The colors show the expected course through increasing pressure and enthalpy levels with the crank angle, the latter being caused by the transient pressure term in Eq. (4). One interesting observation is that the flame speed reduction by the pressure is compensated for by the simultaneous enthalpy increase. This leads to an overall increase of the laminar flame speed throughout the flame propagation besides the acceleration caused by turbulent wrinkling. Furthermore it is important to note the flame thicknesses found throughout the cycle. In conjunction with the modeling outlined above and specifically the resolution requirement given by Eq. (8), a discrepancy to the resolution actual available in the simulation ($\Delta_\mathrm{x} = \mathcal{O}(0.5\,\mathrm{mm})$) must be compensated for by the model.

[Figure 13 about here.]

4. Results

For the evaluation, statistics are gathered for a series of cycles conditioned on the cad. As already outlined in Section 2, within the experiment 300 cycles for each plane are considered where statistical convergence was confirmed. Due to limited resources, the simulation covers only 60 cycles. The convergence analysis based on the measurements revealed that such a subset of 60 cycles mostly suffices for first order moments. At this, the pressure curve quickly converged while the flame propagation still showed some statistical uncertainties. In the following, first in Section 4.1 the measured and computed pressure curves are discussed. Two simulations are considered named *LES1* and *LES2* in the following. *LES1* was conducted first with the default model settings and an estimated flame kernel size at ignition as detailed below. This first simulation underestimated the pressure evolution and the analysis of the results revealed modeling deficiencies which have been corrected in the second simulation (*LES2*) by adjusting parameters according

to their physical interpretation. After the pressure curve evaluation, Section 4.2 compares the measured and simulated flame propagation.

4.1 *Pressure curve and model sensitivity*

[Table 2 about here.]

[Figure 14 about here.]

The results are summarized in Fig. 14 and Table 2. As common for SI engines the measurements show a distinct pressure rise with a certain delay after ignition. The averaged peak pressure is 29.27 bar at 10 cad and the fluctuation added to Fig. 14 increases up to 2.19 bar at 4.5 cad indicating an rms of about 10% compared to the average pressure. Considering the simulation *LES1,* it generally underestimates the pressure evolution. Compared to the measurements it also shows a distinct increase caused by the flame propagation also being at about the same cad, but the slope is visibly lower. Accordingly, the predicted peak pressure is delayed by 6 cad (see table 2). During this delay, the piston proceeded downwards such that the combustion evolves within a larger in-cylinder volume, causing an underestimation of the maximum pressure by 6 bar. Likewise, the ccv indicated by p_{rms} are reduced. It should be noted, that p_{rms} in Fig. 14 does not return to a value of zero for the cad regime shown. This is likely due to reactions taking place during early expansion that involve a fresh mixture outgassing from the relatively large piston crevice volume associated with optical engines. This phenomena has been documented in [64–66]. It is also visible in the simulation but the fluctuation is slightly underestimated probably caused by insufficient resolution of the crevice.

[Figure 15 about here.]

It is important to evaluate the potential differences between experiments and simulations as they may explain the discrepancies in the *LES1* pressure results. Regarding the boundary conditions at the inlet and outlet, the motored case showed that the values provided in the intake and exhaust manifold are well defined and suited for simulations. Engine speed is another parameter with potential discrepancies. The engine speed was assumed to be constant in the simulation. In the experiments, Baum [64] has performed a detailed crank-angle based engine speed analysis. For the engine operating conditions presented in this study, it was demonstrated that the actual engine speed can reduce by up to 5% near the end of compression for fired operation. This problem arises due to a single-mass flywheel inertia change at a relatively low engine speed of 800 RPM. In theory, this gives the flame more time to evolve per cad in the experiment such that the simulation would appear as being delayed. However, for the duration from ignition until the end of combustion (i.e. about 26 cad), this minor reduction in engine speed would only attribute to a 285 μs duration for which the flame would have an additional time to propagate in the experiments and increase the in-cylinder pressure. At most, this would suggest a maximum 1.3 cad lag between experiment and simulation at the peak pressure. Accordingly, this effect would only shift the results slightly closer towards each other and can therefore only explain a small part of the deviation. Likely the major cause is related to the modeling of the combustion process. This process consists of two physical sequences being:

- The ignition until a stable flame kernel formation

- The subsequent (turbulent) flame propagation

With both of these phases major uncertainties of the simulation are associated causing the mismatch between *LES1* and the measurements. Therefore, a systematic study was conducted to understand the sensitivity of their prediction according to modeling parameters related to each of them. Due to the high computational costs it is not possible to perform a full statistical evaluation (i.e. phase averaging of 60 cycles) for each set of modeling parameters. Accordingly, the procedure was to restart the simulation of some representative cycles from their state prior to ignition. This allows to obtain an adequate range of the pressure curve's sensitivity to the modeling parameters that were varied according to their physical significance. Such a map is provided in Fig. 15 and will be detailed with the associated settings of the combustion model in the following.

Considering first the ignition. It is a complex physical process that can only be approximated in simulations. The current approaches must be adjusted to the individual modeling concept (e.g. energy deposition is used for ATF [36], ISSIM model is used for FSD [67]). Within our tabulation approach the ignition is realized by setting a small region at the spark to its burnt state (see Fig. 11) at the instant of spark discharge at -16 cad. It is a relatively simple approach but still widely used (e.g. [32]). After this initial artificial fuel conversion, just like in the real engine, a self-sustaining flame forms that naturally expands in the turbulent flow. Obviously, setting a meaningful kernel size is then a sensitive choice for which generally little reference is available. The impact of the initial kernel size onto the pressure curve is given qualitatively on the left of Fig. 15, where two things can be observed. First, as expected, the combustion evolves quicker with increasing kernel size. However, and second, even though the correct peak can finally be reached, the qualitative course towards it is wrong. While the kernel size has a strong effect onto the early stage after ignition, the strong change in the pressure slope observed in the measurements at about -5 cad is not associated with it. One possible reason for the underestimation of the pressure evolution was an insufficient strong ignition. With these findings this is obviously not the case since an increased kernel size leads to a clear deviation at very early stages where it is the dominant parameter. Furthermore, as indicated by the larger circle in Fig. 11, the kernel size of the *LES1* covers already a significant region and further increasing it seems rather unrealistic. Indeed, the following analysis and the flame imaging discussed in the next section will confirm that the flame front evolution rather corresponds to a smaller kernel and a faster growth.

[Figure 16 about here.]

Considering next the flame propagation. Since this growth rate results from the turbulent flame propagation, these findings shift the attention to the flame-turbulence-interaction partially being modeled within the LES. Naturally, regardless of the model, the flame wrinkling under high pressure cannot be resolved on LES meshes which must be compensated for. In this regard, also Schmitt et al. [32] observed a strong impact related to the estimated turbulent flame speed utilized for the G-Equation approach. As explained in Section 3.2.2 and Fig. 11, within the DTFM, the efficiency function should compensate for the wrinkling suppressed by the thickening. With this approach, Enaux et al. [36] predicted the pressure curve for the SGEmac engine very well. However, their mesh was significantly finer (0.2 mm to 0.4 mm here) while a lower pressure was

considered (20 bar to 30 bar here). Due to both of these differences the amount of unresolved winkling is significantly higher within this simulation, i.e. for a given modeling uncertainty its impact is much larger here. Furthermore, a more complex fuel is considered here but this should be covered well by the tabulation. In summary, the modeled turbulent flame propagation generally can have a large influence and is apparently underestimated by the efficiency function in our simulation. Accordingly, as done for the kernel size, we studied the impact of the modeled unresolved wrinkling onto the pressure curve. It should be noted that the formulation of Eq. (14) itself has been derived based on assumptions whose transferability to engine conditions is uncertain. However, this fundamental question is beyond the scope of this work and we are limited to adjusting the given formulation.

The effect of increasing the modeled part of the turbulent flame propagation is qualitatively shown on the right of Fig. 15. It is clearly visible that it has a significant impact onto the change in slope while the pressure evolution in the early phase is only slightly altered. Accordingly, it can be concluded that the effects of ignition and propagation can be separated into the initial behavior after ignition and the subsequent change in slope, respectively. Likewise, it is possible to attribute the corresponding modeling uncertainties by considering the respective phases.

Instead of a simple scaling of Eq. (14), it is more reasonable to consider the individual uncertainties that enter the efficiency function formulation. Those are the velocity fluctuation u'_Δ and the scaling exponent β. Both of them have been varied based on analyzing $\mathcal{E}$ found in our simulation and the corresponding pressure curves. For this purpose, Fig. 16 and 17 provide some insight into the efficiency function. The top of Fig. 16 shows $\mathcal{E}$ mapped onto an iso-surface of the flame front in *LES1* for a given cad. A more quantitative representation is given in the top left of Fig. 17 showing the PDF of $\mathcal{E}$ along such an iso-surface for several cad. In the early phase after ignition, the PDF shows a broad distribution and one can see that the flame gets strongly accelerated by about a factor of three on average. However, with increasing cad, the distribution continuously shifts towards lower values. On one hand, this is reasonable since the turbulence level reduces during this phase. On the other hand, the flame gets increasingly thinner which in turn requires a larger thickening factor and therewith potentially more unresolved wrinkling to be compensated for.

Considering the velocity fluctuation u'_Δ, it is computed based on the Laplacian of the velocity field (see [63]) to enter the efficiency function. Accordingly, this quantity is sensitive to the turbulent decay following the intake-stroke throughout the compression and flame propagation phases which might be overestimated by the simulation[1]. In this context it is worth noting, that $\mathcal{E}$ as given by Eq. (14) has a theoretical maximum depending on $\mathcal{F}$ via

$$\mathcal{E}_{\max} = (1 + \mathcal{F})^{\beta}\,, \tag{15}$$

i.e. as also visible in Fig. 12, for large values of u'_Δ it converges towards this value. As visible in the bottom left in Fig. 17, where $\mathcal{E}$ is normalized using this quantity, the efficiency function is significantly lower meaning that it is quite plausible that

[1]Plausible causes are an insufficient grid size or an overestimation of the turbulent viscosity.

rather low values of u'_Δ get predicted by the simulation even though a reference for this latter does not exist. Accordingly, it is necessary and justified to rescale the computed fluctuation corresponding to an adjustment of the coefficient c_2 in reference [63]. Regarding the scaling exponent, the *LES1* uses a constant value of $\beta = 0.5$ as suggested by [68]. However, later works [62, 69] where a dynamic formulation has been developed and used also showed larger values even above $\beta = 0.8$.

[Figure 17 about here.]

To summarize the adjustments, appropriate values for the ignition kernel size, u'_Δ and β were obtained to perform the *LES2* as given in Table 2 even though a final conclusion related to the quality of the predicted turbulent flowfield and the suitability of the efficiency formulation cannot be drawn. As already provided on the right of Fig. 15, after increasing the efficiency function also a slight overestimation in the early stage exists which could only be corrected by lowering the initial kernel size (see Table 2 and Fig. 11). Indeed, as we will see in Section 4.2, the flame images confirm that it was assumed too large in the *LES1* simulation. Accordingly, both, the kernel size and the propagation have a certain impact whose adjustments are consistent with the pressure curve and flame imaging. At this, the influence of the kernel size onto the pressure curve is related to the early stage while the propagation speed strongly impacts the slope increase and therewith the qualitative evolution.

To visualize the impact of these adjustments, the corresponding plot of *LES2* is shown in the bottom of Fig. 16. To be comparable, both of these simulations have been ignited starting from the same initial turbulent field. Accordingly, the geometric iso-surfaces are very similar since they mostly result from the resolved wrinkling being identical in both simulations. However, as the color indicates, the flame of *LES2* propagates significantly faster. Accordingly, the flame ball is larger which is not so visible in this three-dimensional view but will be detailed in Section 4.2. The corresponding PDFs are given on the right of Fig 17 where two observations can be made. First, as forced by the modifications, larger values occur but as for the *LES1,* the PDF shifts towards lower values during the combustion process. Second, also the PDF shape changed, specifically the reduction with increasing cad is delayed and here even the larger cads show a large contribution of very high values of $\mathcal{E}$. Finally, with these settings, 60 cycles of the *LES2* have been averaged and the results have been added to Fig. 14 and Table 2. One can see, that this modification enables the simulation to very accurately predict the measured pressure not only its average value, but also its fluctuation.

4.2 *Flame propagation*

[Figure 18 about here.]

To provide further insight into the combustion process, we now consider the flame propagation in more detail. While the pressure is rather a global indicator for the integral fuel consumption, this allows one to judge on the local flame position. First, the simulation results of *LES2* will be used to qualitatively outline the process of the flame propagation within this engine using Fig. 18-22. Figure 18 gives an illustration of the flame propagation starting from the initial kernel that expands with increasing flame wrinkling and finally reaches the walls. This

kernel expansion is a superposition of the turbulent flame propagation and flow convection as detailed in Fig. 19. It shows the swirl plane whose position is illustrated in Fig. 4. The streamlines indicate the mean velocity field crossing the flame kernel given in red. One can see, that there is a mean flow towards the negative x-direction that will convect the flame kernel while it is expanding as illustrated in Fig. 20. The left shows the phase-averaged progress variable by means of one iso-contour per cad. An interesting observation is that the flame kernel is relatively circular meaning that it propagates in each direction at a similar speed while it is being convected to the left by the mean flow. For illustrative purpose a corresponding single cycle is shown on the right. As in Fig. 18, one can see that the flame increases its wrinkling throughout the propagation and can be strongly asymmetrical. The same illustrations are given in Fig. 21 and 22 within the tumble plane whose position is also marked in Fig. 4. A slightly later cad has been chosen in Fig. 22 where the interaction of the velocity field in the region of the spark plug and the propagation is clearly visible. A more qualitative discussion will be given below jointly with the measurements.

[Figure 19 about here.]

[Figure 20 about here.]

The propagation can strongly vary from cycle-to-cycle as visualized in Fig. 23 and 24. Especially in the swirl-plane one can see that, for a given crank angle, the flame shapes of different cycles are not only different regarding the local wrinkling, but also cover globally very different regions, while the averaged propagation represents a relatively smooth and symmetric shape. The effect of the increased efficiency function onto the instantaneous flame propagation is given in Fig. 25. It compares the flame positions as predicted by the *LES1* and *LES2*. As for the comparison in Fig. 16 they are ignited from the same initial field and accordingly show a similar geometric shape. At 2 cad the flame of the *LES2* covers a much larger area and its radial extent exceeds the *LES1* at almost all positions. From the perspective of this 2D viewing plane the *LES2* has only small unburnt pockets while the *LES1* rather shows individual burnt gas islands. At 4 cad, these islands then unite within the process of the flame kernel growth but the delay compared to the *LES2* is very visible.

[Figure 21 about here.]

[Figure 22 about here.]

[Figure 23 about here.]

[Figure 24 about here.]

[Figure 25 about here.]

Finally, going over to the characterization of the flame propagation using the experimental imaging in the tumble- and swirl-plane, the evaluation and comparison with the simulations is given in Fig. 27-31. Due to the limited field of view in the experiments (see Fig. 4), rather early instants being at -10, -6 and -2 cad are shown. The corresponding pressure evolution during these instants is given in Fig. 26. The measured kernel expansion is given in the left column of Fig. 27 and 29 for the tumble- and swirl-plane, respectively. In these figures the

color represents the phase averaged probability of the burnt gas region to visualize the progress of the flame. As one can see in the tumble plane measurements, right after ignition the flame kernel quickly moves towards the negative x-direction due to convection by the flow. Also the piston is quickly approached while the fresh gases towards the positive x-direction are consumed later by the flame propagation. Accordingly, for the x-direction the same behavior is visible within the swirl plane, while the expansion in the y-direction is relatively symmetrical since the in-cylinder flow has no swirling motion.

[Figure 26 about here.]

[Figure 27 about here.]

[Figure 28 about here.]

[Figure 29 about here.]

[Figure 30 about here.]

The simulation results are given in the middle and right column for the *LES1* and *LES2* in Fig. 27 and 29, respectively. Besides this visualization by means of the burnt gas PDFs, Fig. 28 and 30 provide a more quantitative comparison of the flame positions by using $\bar{c} = 0.5$ iso-contours. Starting with the *LES1*, we already mentioned that the comparison of the averaged flame position revealed that the initial kernel size was set too large. Within both the swirl and tumble plane, the flame is ahead of the experiments at -10 cad but shows a very similar convection towards the negative x-direction. In this early phase the flame imaging is vital to assess the simulation, i.e. as Fig. 26 indicates the effect onto the pressure is not significant, but the flame deviations are clearly visible from the green curves in Fig. 28. The further two instants being at -6 cad and -2 cad then provide the complete picture of the simulations deficiency. At -6 cad the predicted flame position is close to the measured one while it shows an insufficient kernel expansion at -2 cad: in the tumble plane both approached the piston head but the simulated flame propagates too slowly in the positive x-direction. In the swirl-plane, in most of the regions the overall flame ball is too small primarily towards the y-direction. This evolution is reflected in the pressure curve (Fig. 26). At -6 cad the measurements cross the simulation while a first significant difference is visible at -2 cad. This latter arises by the strong slope increase at about -5 cad where the influence of the flame propagation onto the pressure curve starts to become significant, i.e. the deviations of *LES1* are clearly attributed to an insufficient propagation speed whose effect is not yet very significant at -6 cad where partial compensation with the ignition model takes place.

Going over to the *LES2,* just as for the pressure curve, also the predicted burnt gas region is in better agreement with the experimental findings. In the tumble plane (Fig. 28), at -10 cad, the burnt gas comprises of a small area left of the spark plug close to the one seen in the experiments. This agreement, found at 6 cad after ignition, supports the use of the smaller initial kernel size even though the simulated flame extents slightly further downwards such that it is already visible in the swirl plane not yet reached in the measurements. At -6 cad, the burnt gas area remains slightly larger than seen in the experiments in that it covers a larger region to the right of the spark plug. Considering the further evolution found at -2 cad, the burnt gas area agrees well with experiments, covering nearly the same regions. Here, the

images as well as the pressure curve confirm that the faster burning predicted by the *LES2* provides a more accurate rate of the pressure rise and flame propagation.

Finally, a further comparison is provided in Fig. 31 where the normalized reaction progress variable is plotted along the lines indicated in green in Fig. 29. This allows to evaluate its spatial evolution in addition to the single contour given in Fig. 28 and 30. The transition from the unburnt to the burnt state represents the turbulent flame brush in a phase-averaged sense. Along the x-direction at -6 cad the left slope is predicted quite accurately while a certain discrepancy exists towards positive x-positions where the flame propagation is very sensitive to the flow around the spark plug. At -2 cad only the *LES2* is in satisfactory agreement with the experiments while the *LES1* underestimates the slope and not even reaches the fully burnt state as the measurements indicate with a large $\bar{c} = 1$ region. In the y-direction the shape for both cad considered is very accurately predicted by the *LES2*.

[Figure 31 about here.]

5. Summary and conclusion

This work considered experiments and simulations of the fired operation of an optically accessible spark ignition engine. From the measurements a database was derived to characterize the process by means of the pressure curve and a flame imaging technique. The latter provided a detailed view of the flame propagation within the swirl and tumble plane.

Within the simulations conducted we showed the application of the DTFM combined with pressure-dependent FGM tabulation of pre-computed thermo-chemical states using detailed chemistry. At this, we first demonstrated the functionality of the tabulation approach when embedded into the ALE-scheme of the LES code. The method has then been applied to the engine and a comparison based on phase-averaged data was conducted. The comparison revealed a certain discrepancy to the measurements which has been analyzed and could be related to modeling uncertainties. Within this analysis, the flame imaging allowed a clear differentiation between errors in the ignition and the propagation. Based on these findings we adjusted the modeling parameters which enabled the simulation in a second run to quite accurately reproduce the measurements in both, the pressure and the flame shape. An interesting observation is that the adjustments did not only improve the agreement with the averaged pressure but also the fluctuations that represent the intensity of the cycle-to-cycle variations.

Within this work the joint utilization of experiments and simulation data gave access to valuable information on the actual flame shape regarding its spatial and temporal evolution. The primary focus was to show that the imaging technique can serve as a well suited method to analyze the simulation quality and identify modeling deficiencies and necessary adjustments. Furthermore, a first view on the flame propagation mechanism was provided. For future works, the consideration of other engine conditions would be valuable to assess the generality of the conclusions and provide further physical insight.

Acknowledgments

We gratefully acknowledge financial support by the German Research Council (DFG) through the SFB/Transregio 150 and the *Graduate School of Computational Engineering (GSC 233)* in Darmstadt. Computations have been performed on the Lichtenberg High Performance Computer of TU Darmstadt, member of HPC Hessen. We would like to thank Andreas Dreizler from TU-Darmstadt for helpful discussions.

References

[1] A. Alagumalai, Internal combustion engines: Progress and prospects, Renewable and Sustainable Energy Reviews 38 (2014) 561–571.

[2] R. D. Reitz, G. Duraisamy, Review of high efficiency and clean reactivity controlled compression ignition (RCCI) combustion in internal combustion engines, Progress in Energy and Combustion Science 46 (2015) 12–71.

[3] T. D. Fansler, D. L. Reuss, V. Sick, R. N. Dahms, Invited Review: Combustion instability in spray-guided stratified-charge engines: A review, International Journal of Engine Research 16 (2015) 260–305.

[4] F. Zhao, M. C. Lai, D. L. Harrington, Automotive spark-ignited direct-injection gasoline engines, Progress in Energy and Combustion Science 25 (1999) 437–562.

[5] V. Gheorghiu, Ultra-Downsizing of Internal Combustion Engines, in: A. Subic, J. Wellnitz, M. Leary, L. Koopmans (Eds.), Sustainable Automotive Technologies 2012: Proceedings of the 4th International Conference, Springer Berlin Heidelberg, Berlin, Heidelberg, 2012, pp. 145–155.

[6] H. Zhao, HCCI and CAI Engines for the Automotive Industry, Woodhead Pub, Boca Raton FL; Cambridge, England, new. edition, 2007.

[7] C. Hasse, Scale-resolving simulations in engine combustion process design based on a systematic approach for model development, International Journal of Engine Research 17 (2016) 44–62.

[8] A. Dreizler, B. Böhm, Advanced laser diagnostics for an improved understanding of premixed flame-wall interactions, Proceedings of the Combustion Institute 35 (2015) 37–64.

[9] V. Sick, M. C. Drake, T. D. Fansler, High-speed imaging for direct-injection gasoline engine research and development, Experiments in Fluids 49 (2010) 937–947.

[10] V. Sick, High speed imaging in fundamental and applied combustion research, Proceedings of the Combustion Institute 34 (2013) 3509–3530.

[11] M. C. Drake, D. C. Haworth, Advanced gasoline engine development using optical diagnostics and numerical modeling, Proceedings of the Combustion Institute 31 (2007) 99–124.

[12] A. Misdariis, A. Robert, O. Vermorel, S. Richard, T. Poinsot, Numerical Methods and Turbulence Modeling for LES of Piston Engines: Impact on Flow Motion and Combustion, Oil & Gas Science and Technology 69 (2014) 83–105.

[13] K. Zha, S. Busch, P. C. Miles, S. Wijeyakulasuriya, S. Mitra, P. K. Senecal, Characterization of Flow Asymmetry During the Compression Stroke Using Swirl-Plane PIV in a Light-Duty Optical Diesel Engine with the Re-entrant Piston Bowl Geometry, SAE International Journal of Engines 8 (2015).

[14] P. C. Miles, B. H. Rempel Ewert, R. D. Reitz, Experimental assessment of a nonlinear turbulent stress relation in a complex reciprocating engine flow, Experiments in Fluids 47 (2009) 451–461.

[15] M. C. Drake, T. D. Fansler, A. M. Lippert, Stratified-charge combustion: modeling and imaging of a spray-guided direct-injection spark-ignition engine, Proceedings of the Combustion Institute 30 (2005) 2683–2691.

[16] T. D. Fansler, M. C. Drake, B. Böhm, High-speed Mie scattering diagnostics for spray-guided gasoline engine development, in: AVL Europe, Wiesbaden, 2008.

[17] P. Schiffmann, S. Gupta, D. Reuss, V. Sick, X. Yang, T.-W. Kuo, TCC-III Engine Benchmark for Large-Eddy Simulation of IC Engine Flows, Oil & Gas Science and Technology 71 (2016) 3.

[18] P. Abraham, K. Liu, D. Haworth, D. Reuss, V. Sick, Evaluating Large-Eddy Simulation (LES) and High-Speed Particle Image Velocimetry (PIV) with Phase-Invariant Proper Orthogonal

Decomposition (POD), Oil & Gas Science and Technology 69 (2014) 41–59.

[19] C. Lacour, C. Pera, An Experimental Database Dedicated to the Study and Modelling of Cyclic Variability in Spark-Ignition Engines with LES, SAE Technical Paper, SAE Technical Paper, 2011.

[20] E. Baum, B. Peterson, B. Böhm, A. Dreizler, On The Validation of LES Applied to Internal Combustion Engine Flows: Part 1: Comprehensive Experimental Database, Flow, Turbulence and Combustion 92 (2013) 269–297.

[21] F. Zentgraf, E. Baum, B. Böhm, A. Dreizler, B. Peterson, On the turbulent flow in piston engines: Coupling of statistical theory quantities and instantaneous turbulence, Physics of Fluids 28 (2016).

[22] B. Peterson, E. Baum, B. Böhm, A. Dreizler, Early flame propagation in a spark-ignition engine measured with quasi 4d-diagnostics, Proceedings of the Combustion Institute 35 (2015) 3829–3837.

[23] F. Perini, K. Zha, S. Busch, P. Miles, R. D. Reitz, Principal Component Analysis and Study of Port-Induced Swirl Structures in a Light-Duty Optical Diesel Engine, SAE Technical Paper, SAE Technical Paper, 2015.

[24] R. N. Dahms, M. C. Drake, T. D. Fansler, T. W. Kuo, N. Peters, Understanding ignition processes in spray-guided gasoline engines using high-speed imaging and the extended spark-ignition model SparkCIMM. Part A: Spark channel processes and the turbulent flame front propagation, Combustion and Flame 158 (2011) 2229–2244.

[25] R. N. Dahms, M. C. Drake, T. D. Fansler, T. W. Kuo, N. Peters, Understanding ignition processes in spray-guided gasoline engines using high-speed imaging and the extended spark-ignition model SparkCIMM: Part B: Importance of molecular fuel properties in early flame front propagation, Combustion and Flame 158 (2011) 2245–2260.

[26] R. Dahms, T. D. Fansler, M. C. Drake, T. W. Kuo, A. M. Lippert, N. Peters, Modeling ignition phenomena in spray-guided spark-ignited engines, Proceedings of the Combustion Institute 32 (2009) 2743–2750.

[27] R. Dahms, C. Felsch, O. Röhl, N. Peters, Detailed chemistry flamelet modeling of mixed-mode combustion in spark-assisted HCCI engines, Proceedings of the Combustion Institute 33 (2011) 3023–3030.

[28] K. Liu, D. C. Haworth, X. Yang, V. Gopalakrishnan, Large-eddy Simulation of Motored Flow in a Two-valve Piston Engine: POD Analysis and Cycle-to-cycle Variations, Flow, Turbulence and Combustion 91 (2013) 373–403.

[29] C. J. Rutland, Large-eddy simulations for internal combustion engines a review, International Journal of Engine Research 12 (2011) 421–451.

[30] S. Richard, O. Colin, O. Vermorel, A. Benkenida, C. Angelberger, D. Veynante, Towards large eddy simulation of combustion in spark ignition engines, Proceedings of the Combustion Institute 31 (2007) 3059–3066.

[31] K. Truffin, C. Angelberger, S. Richard, C. Pera, Using large-eddy simulation and multivariate analysis to understand the sources of combustion cyclic variability in a spark-ignition engine, Combustion and Flame 162 (2015) 4371–4390.

[32] M. Schmitt, R. Hu, Y. M. Wright, P. Soltic, K. Boulouchos, Multiple Cycle LES Simulations of a Direct Injection Natural Gas Engine, Flow, Turbulence and Combustion 95 (2015) 645–668.

[33] B. Enaux, V. Granet, O. Vermorel, C. Lacour, L. Thobois, V. Dugu, T. Poinsot, Large Eddy Simulation of a Motored Single-Cylinder Piston Engine: Numerical Strategies and Validation, Flow, Turbulence and Combustion 86 (2010) 153–177.

[34] D. C. Haworth, Progress in probability density function methods for turbulent reacting flows, Progress in Energy and Combustion Science 36 (2010) 168–259.

[35] A. Banaeizadeh, A. Afshari, H. Schock, F. Jaberi, Large-eddy simulations of turbulent flows in internal combustion engines, International Journal of Heat and Mass Transfer 60 (2013) 781–796.

[36] B. Enaux, V. Granet, O. Vermorel, C. Lacour, C. Pera, C. Angelberger, T. Poinsot, LES study of cycle-to-cycle variations in a spark ignition engine, Proceedings of the Combustion Institute 33 (2011) 3115–3122.

[37] S. Demesoukas, C. Caillol, P. Higelin, A. Boiarciuc, A. Floch, Near wall combustion modeling in spark ignition engines. Part A: Flame-wall interaction, Energy Conversion and Management 106 (2015) 1426–1438.

[38] G. Lecocq, S. Richard, J.-B. Michel, L. Vervisch, A new LES model coupling flame surface density and tabulated kinetics approaches to investigate knock and pre-ignition in piston engines, Proceedings of the Combustion Institute 33 (2011) 3105–3114.

[39] A. Misdariis, O. Vermorel, T. Poinsot, LES of knocking in engines using dual heat transfer and two-step reduced schemes, Combustion and Flame 162 (2015) 4304–4312.

[40] A. Robert, S. Richard, O. Colin, L. Martinez, L. De Francqueville, LES prediction and analysis of knocking combustion in a spark ignition engine, Proceedings of the Combustion Institute 35 (2015) 2941–2948.

[41] C. Pera, O. Colin, S. Jay, Development of a FPI Detailed Chemistry Tabulation Methodology for Internal Combustion Engines, Oil & Gas Science and Technology - Rev. IFP 64 (2009) 243–258.

[42] C. Bekdemir, L. M. T. Somers, L. P. H. de Goey, Modeling diesel engine combustion using pressure dependent Flamelet Generated Manifolds, Proceedings of the Combustion Institute 33 (2011) 2887–2894.

[43] V. Granet, O. Vermorel, C. Lacour, B. Enaux, V. Dugu, T. Poinsot, Large-Eddy Simulation and experimental study of cycle-to-cycle variations of stable and unstable operating points in a spark ignition engine, Combustion and Flame 159 (2012) 1562–1575.

[44] R. Evans, L., Lean-Burn Spark-Ignited Internal Combustion Engines, in: Lean Combustion: Technology and Control, Elsevier, Inc., 2008, pp. 95–120.

[45] M. Baumann, F. d. Mare, J. Janicka, On the Validation of Large Eddy Simulation Applied to Internal Combustion Engine Flows Part II: Numerical Analysis, Flow, Turbulence and Combustion 92 (2013) 299–317.

[46] P. Janas, I. Wlokas, B. Böhm, A. Kempf, On the Evolution of the Flow Field in a Spark Ignition Engine, Flow, Turbulence and Combustion (2016) 1–28.

[47] T. M. Nguyen, F. Proch, I. Wlokas, A. M. Kempf, Large Eddy Simulation of an Internal Combustion Engine Using an Efficient Immersed Boundary Technique, Flow, Turbulence and Combustion 97 (2015) 191–230.

[48] D. Freudenhammer, B. Peterson, C.-P. Ding, B. Boehm, S. Grundmann, The Influence of Cylinder Head Geometry Variations on the Volumetric Intake Flow Captured by Magnetic Resonance Velocimetry, SAE International Journal of Engines 8 (2015) 1826–1836.

[49] B. Peterson, D. L. Reuss, V. Sick, High-speed imaging analysis of misfires in a spray-guided direct injection engine, Proceedings of the Combustion Institute 33 (2011) 3089–3096.

[50] B. Peterson, V. Sick, High-speed flow and fuel imaging study of available spark energy in a spray-guided direct-injection engine and implications on misfires, International Journal of Engine Research 11 (2010) 313–329.

[51] B. Peterson, D. L. Reuss, V. Sick, On the ignition and flame development in a spray-guided direct-injection spark-ignition engine, Combustion and Flame 161 (2014) 240–255.

[52] KIVA, KIVA-4mpi, `https://lanl.gov/projects/feynman-center/technologies/software/kiva/index.php`.

[53] D. J. Torres, M. F. Trujillo, KIVA-4: An unstructured ALE code for compressible gas flow with sprays, Journal of Computational Physics 219 (2006) 943–975.

[54] G. Kuenne, A. Ketelheun, J. Janicka, LES modeling of premixed combustion using a thickened flame approach coupled with FGM tabulated chemistry, Combustion and Flame 158 (2011) 1750–1767.

[55] J. A. van Oijen, L. P. H. de Goey, Modelling of Premixed Laminar Flames using Flamelet-Generated Manifolds, Combustion Science and Technology 161 (2000) 113–137.

[56] A. Ketelheun, G. Kuenne, J. Janicka, Heat Transfer Modeling in the Context of Large Eddy Simulation of Premixed Combustion with Tabulated Chemistry, Flow, Turbulence and Combustion 91 (2013) 867–893.

[57] G. Blanquart, P. Pepiot-Desjardins, H. Pitsch, Chemical mechanism for high temperature combustion of engine relevant fuels with emphasis on soot precursors, Combustion and Flame 156 (2009) 588–607.

[58] CHEM1D, A one-dimensional laminar flame code, developed at Eindhoven University of Technology, `www.combustion.tue.nl/chem1d`.

[59] L. P. H. de Goey, J. H. M. ten Thije Boonkkamp, A flamelet description of premixed laminar flames and the relation with flame stretch, Combustion and Flame 119 (1999) 253–271.

[60] J. A. van Oijen, G. Groot, R. J. M. Bastiaans, L. P. H. de Goey, A flamelet analysis of the burning velocity of premixed turbulent expanding flames, Proceedings of the Combustion Institute 30 (2005) 657–664.

[61] J. A. van Oijen, R. J. M. Bastiaans, L. P. H. de Goey, Low-dimensional manifolds in direct numerical simulations of premixed turbulent flames, Proceedings of the Combustion Institute 31 (2007) 1377–1384.

[62] F. Charlette, C. Meneveau, D. Veynante, A power-law flame wrinkling model for LES of premixed turbulent combustion Part II: dynamic formulation, Combustion and Flame 131

(2002) 181–197.

[63] O. Colin, F. Ducros, D. Veynante, T. Poinsot, A thickened flame model for large eddy simulations of turbulent premixed combustion, Physics of Fluids 12 (2000) 1843–1863.

[64] E. Baum, Laserbasierte Untersuchung innermotorischer Prozesse, Ph.D. thesis, TU-Darmstadt, Darmstadt, 2013.

[65] B. Peterson, E. Baum, B. Böhm, V. Sick, A. Dreizler, Evaluation of toluene LIF thermometry detection strategies applied in an internal combustion engine, Applied Physics B 117 (2014) 151–175.

[66] M. Gleiner, Analyse von Brennraumströmung, Gemischbildung und Verbrennung am Transparentmotor mit Benzindirekteinspritzung und strahlgeführtem Brennverfahren, Ph.D. thesis, TU-Darmstadt, Darmstadt, 2011.

[67] O. Colin, K. Truffin, A spark ignition model for large eddy simulation based on an FSD transport equation (ISSIM-LES), Proceedings of the Combustion Institute 33 (2011) 3097–3104.

[68] F. Charlette, C. Meneveau, D. Veynante, A power-law flame wrinkling model for LES of premixed turbulent combustion Part I: non-dynamic formulation and initial tests, Combustion and Flame 131 (2002) 159–180.

[69] G. Wang, M. Boileau, D. Veynante, Implementation of a dynamic thickened flame model for large eddy simulations of turbulent premixed combustion, Combustion and Flame 158 (2011) 2199–2213.

List of figure captions

Figure 1: Optically accessible engine with the measurement points and extent of the computational domain.

Figure 2: Top: in-cylinder pressure of the acquired measurements and valve lift. Middle and bottom: Pressure measured in the intake and exhaust manifold and the corresponding standard deviation.

Figure 3: Average and standard deviation of the magnitude and cad of maximum pressure for the evaluated runs. Red indicates a single run with 100 evaluated cycles without seeded oil droplets.

Figure 4: Experimental setup used for flame position detection. Green color indicates the setup used for the horizontal plane, red color indicates the vertical plane measurements.

Figure 5: Raw images illustrating the flame detection at specified cad for the tumble plane (left, y=0 mm) and swirl plane (right, z=1.8 mm being 1.4mm below the spark plug). Due to reflections, burnt regions are harder to identify in the swirl plane.

Figure 6: Evolution of the pressure for the motored case.

Figure 7: Surface approximation by the numerical mesh.

Figure 8: Top: Numerical grid depicting the intake flow velocity in the y = -19 mm plane. Bottom: numerical grid depicting the early flame kernel position (via temperature distribution) during late compression in the y = 0 mm plane.

Figure 9: Section of the chemistry table: chemical source term ($kg/(m^3s)$) as a function of the three table access parameters. Iso-surfaces at 30000, 50000 and 70000.

Figure 10: Comparison of one-dimensional flame properties using detailed chemistry (CHEM1D, circles) and tabulated chemistry (KIVA, lines), $\phi = 0.8$. Top: flame speed for conditions during flame propagation. Bottom: flame structure represented by the temperature and the progress variable's chemical source term ($T_\mathrm{u} = 590\,\mathrm{K}$, $p = 15\,\mathrm{bar}$).

Figure 11: Schematic illustration of the flame propagation as modeled in the ATF context. Initial flame kernel sizes, as referred to in Section 4.1, are visually shown at the spark plug (large: *LES1,* small: *LES2,* see Table 2).

Figure 12: Dependency of the efficiency function $\mathcal{E}$ on its input parameters $\mathcal{F}$ and u'_Δ.

Figure 13: Contour: flame thickness δ based on the temperature gradient; Lines: laminar flame speed (cm/s); Circles: states at the flame front during the flame kernel expansion colored by cad.

Figure 14: Comparison of the measured and simulated mean and fluctuating part

of the pressure.

Figure 15: Qualitative illustration showing the influence of the modeled ignition kernel size (left) and flame propagation (right) onto the pressure evolution.

Figure 16: Iso-surface of the flame front colored with the efficiency function showing the effect of increased modeled subgrid winkling. Snapshot of a representative cycle at -2 cad.

Figure 17: Probability distribution of the efficiency function extracted along the flame front for different cad. Top: $\mathcal{E}$; bottom: $(\mathcal{E}-1)/(\mathcal{E}_{\max}-1)$.

Figure 18: Turbulent flame propagation showing a single representative flame kernel expansion from *LES2.* The flame is visualized by an iso-surface of the progress variable (c=0.5) starting at 2 cad after ignition.

Figure 19: Averaged streamlines in the swirl plane superimposed onto the flame contour (progress variable showing the flame kernel in red) at an early stage after ignition (-10 cad). The spark plug being above the plane has been added for orientation (black).

Figure 20: Flame contour in the swirl plane for several cad. Left: averaged; right: single cycle. The spark plug being above the plane has been added for orientation (gray).

Figure 21: Averaged streamlines in the tumble plane superimposed onto the flame contour (progress variable showing the flame kernel in red) at an early stage after ignition (-6 cad).

Figure 22: Flame contour in the tumble plane for several cad. Top: averaged; bottom: single cycle. Compared to Fig. 20 also contains smaller kernels (-14 cad and -12 cad) that did not yet reach the swirl plane.

Figure 23: Illustration of the flame propagation in the tumble plane for cad=-6 (top) and cad=-2 (bottom). Flame position for two individual cycles (colored lines) and time averaged burnt gas region (green).Left: experiments, right: simulation.

Figure 24: Illustration of the flame propagation in the swirl plane for cad=-6 (top) and cad=-2 (bottom). Flame position for two individual cycles (colored lines) and time averaged burnt gas region (green).Left: experiments, right: simulation.The spark plug being above the plane has been added for orientation (gray).

Figure 25: Comparison of the flame propagation within the swirl-plane as predicted by the *LES1* (filled area) and *LES2* (red curve). The spark plug being above the plane has been added for orientation (gray).

Figure 26: Magnified region of the pressure curve showing the section considered for the flame imaging.

Figure 27: Averaged normalized reaction progress variable $\bar{c}$ within the tumble plane. Contour of the experiment (left), *LES1* (middle) and *LES2* (right).

Figure 28: Iso-contour of $\bar{c} = 0.5$ for the corresponding cad at -10 (green), -6 (red) and -2 (blue) for the simulation (solid line) and the experiment (dashed line), respectively. *LES1* (top) and *LES2* (bottom).

Figure 29: As in Fig. 27 but for the swirl plane being at z=1.3 mm. Holes in the measurements are due to reflections.

Figure 30: As in Fig. 28 but for the swirl plane being at z=1.3 mm. The spark plug being above the plane has been added for orientation (gray).

Figure 31: Averaged normalized reaction progress variable extracted along the lines as indicated in green in Fig. 29 for -6 (black) and -2 cad (red). The positions have been chosen to be outside reflections. Circle: experiment; dashed line: *LES1;* solid line: *LES2.*

List of table captions

Table 1: Engine operating conditions. Crank Angle Degrees (cad) are relative to Top-Dead-Center.

Table 2: Parameters of the two simulations and summary of the predicted pressure.

List of Figures

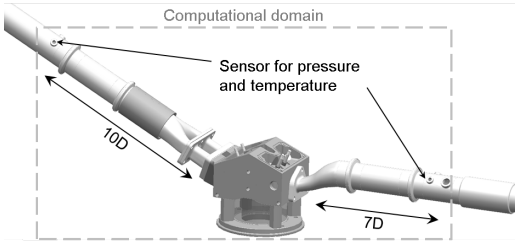

Figure 1. Optically accessible engine with the measurement points and extent of the computational domain.

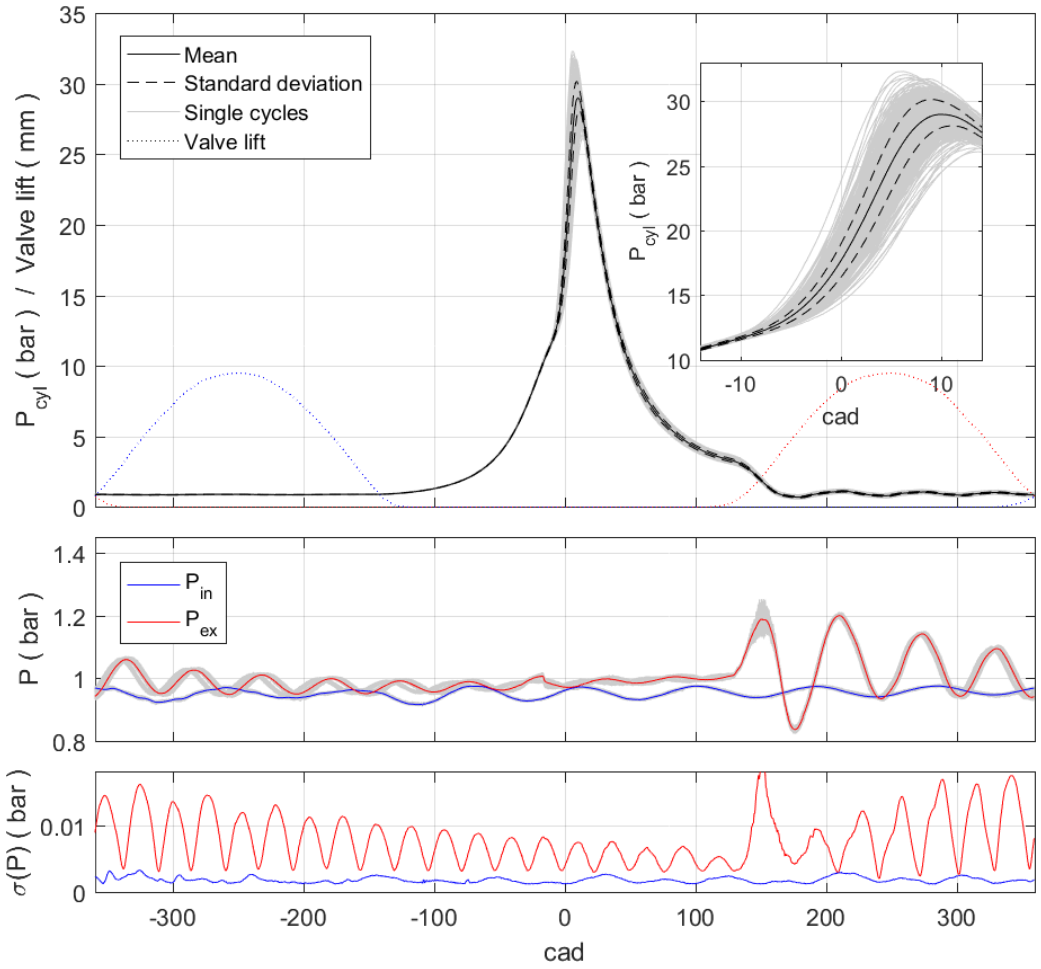

Figure 2. Top: in-cylinder pressure of the acquired measurements and valve lift. Middle and bottom: Pressure measured in the intake and exhaust manifold and the corresponding standard deviation.

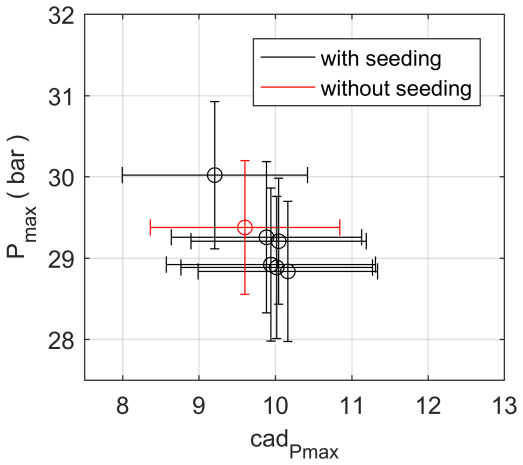

Figure 3. Average and standard deviation of the magnitude and cad of maximum pressure for the evaluated runs. Red indicates a single run with 100 evaluated cycles without seeded oil droplets.

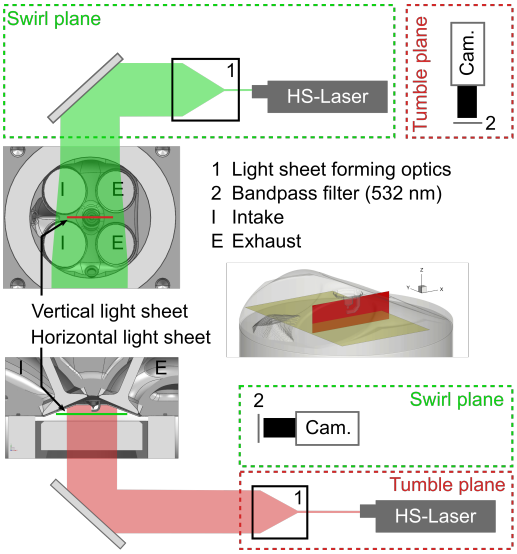

Figure 4. Experimental setup used for flame position detection. Green color indicates the setup used for the horizontal plane, red color indicates the vertical plane measurements.

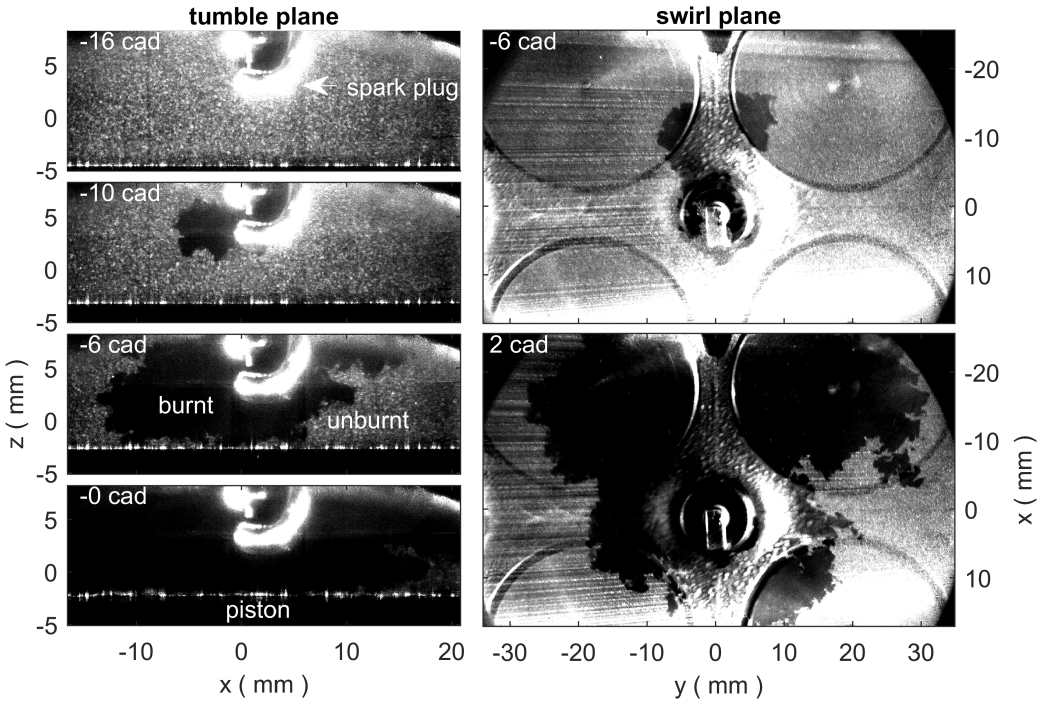

Figure 5. Raw images illustrating the flame detection at specified cad for the tumble plane (left, y=0 mm) and swirl plane (right, z=1.8 mm being 1.4mm below the spark plug). Due to reflections, burnt regions are harder to identify in the swirl plane.

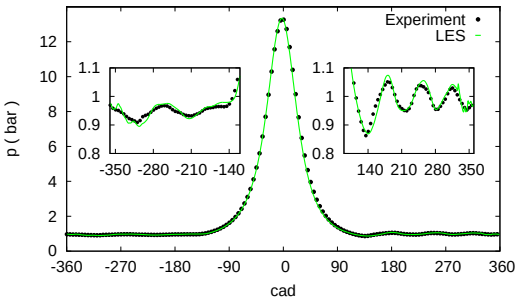

Figure 6. Evolution of the pressure for the motored case.

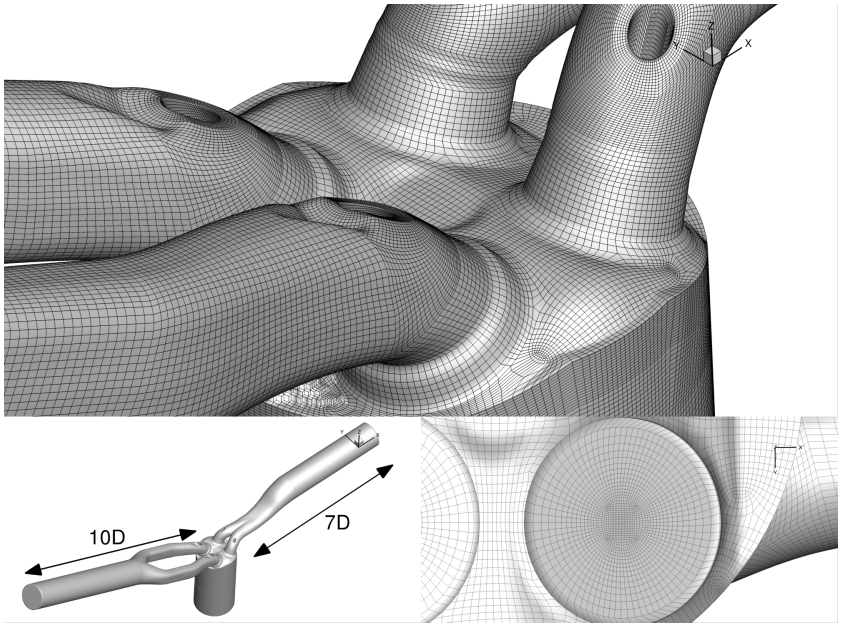

Figure 7. Surface approximation by the numerical mesh.

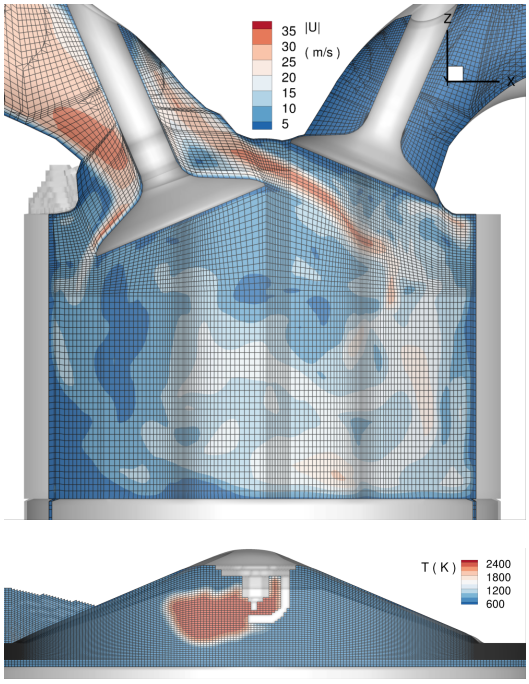

Figure 8. Top: Numerical grid depicting the intake flow velocity in the y = -19 mm plane. Bottom: numerical grid depicting the early flame kernel position (via temperature distribution) during late compression in the y = 0 mm plane.

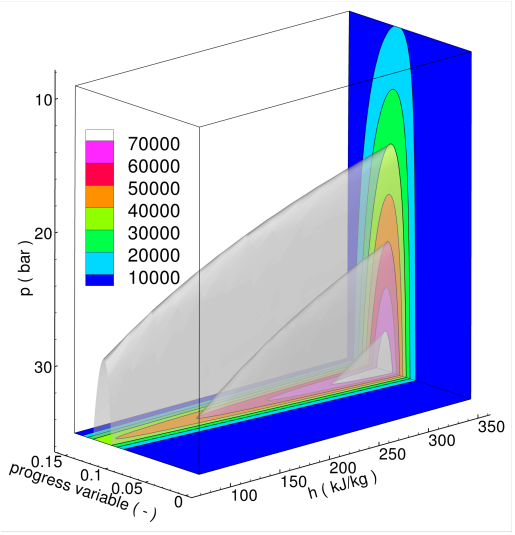

Figure 9. Section of the chemistry table: chemical source term (kg/(m^{3}s)) as a function of the three table access parameters. Iso-surfaces at 30000, 50000 and 70000.

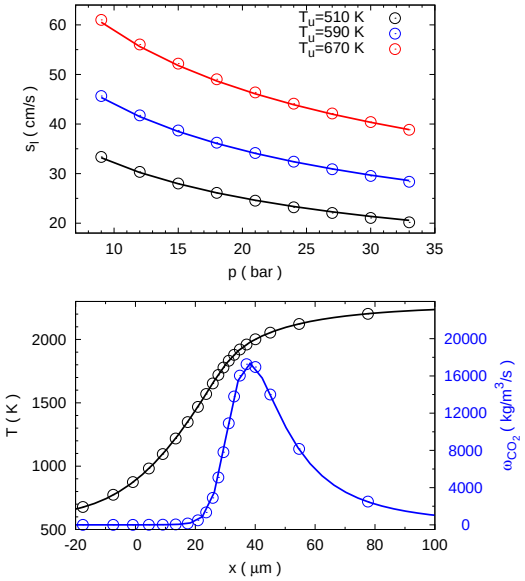

Figure 10. Comparison of one-dimensional flame properties using detailed chemistry (CHEM1D, circles) and tabulated chemistry (KIVA, lines), $\phi = 0.8$. Top: flame speed for conditions during flame propagation. Bottom: flame structure represented by the temperature and the progress variable's chemical source term ($T_\mathrm{u} = 590\,\mathrm{K}$, $p = 15\,\mathrm{bar}$).

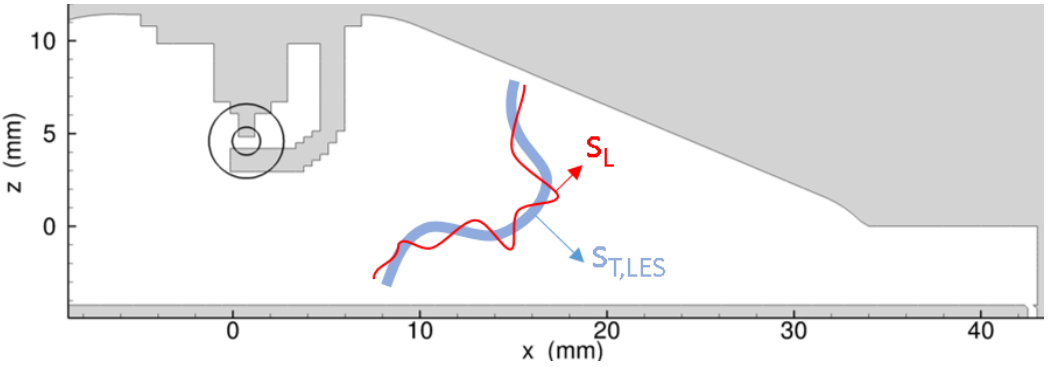

Figure 11. Schematic illustration of the flame propagation as modeled in the ATF context. Initial flame kernel sizes, as referred to in Section 4.1, are visually shown at the spark plug (large: *LES1,* small: *LES2,* see Table 2).

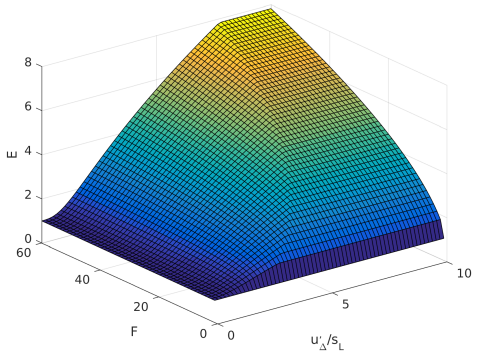

Figure 12. Dependency of the efficiency function $\mathcal{E}$ on its input parameters $\mathcal{F}$ and u'_Δ.

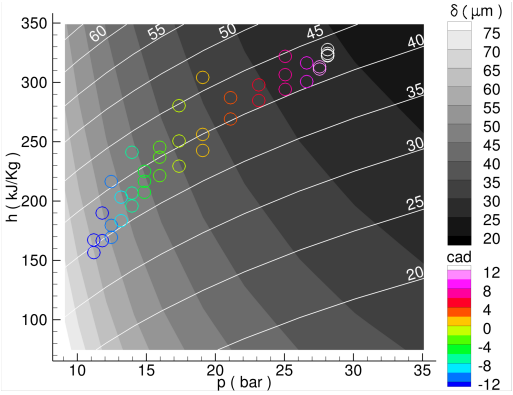

Figure 13. Contour: flame thickness δ based on the temperature gradient; Lines: laminar flame speed (cm/s); Circles: states at the flame front during the flame kernel expansion colored by cad.

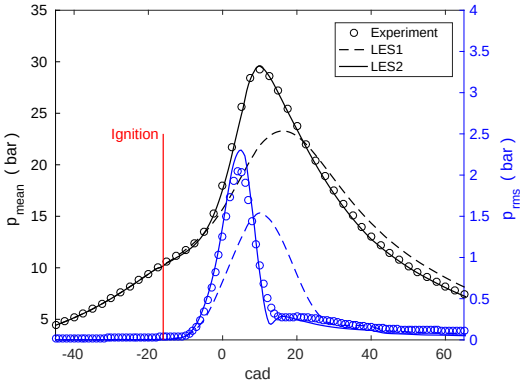

Figure 14. Comparison of the measured and simulated mean and fluctuating part of the pressure.

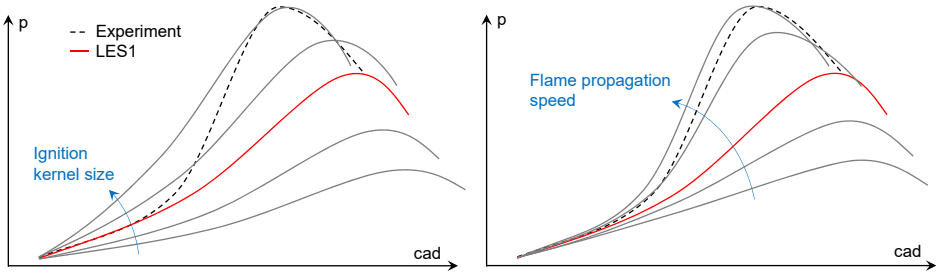

Figure 15. Qualitative illustration showing the influence of the modeled ignition kernel size (left) and flame propagation (right) onto the pressure evolution.

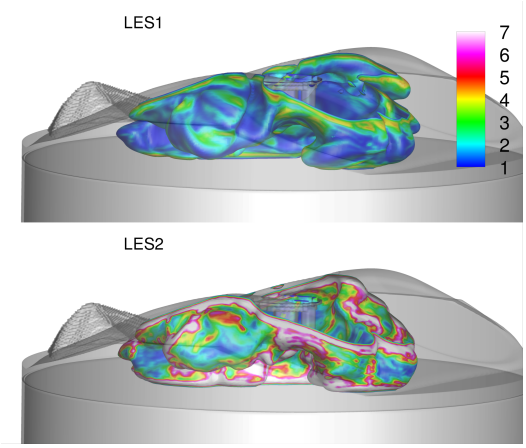

Figure 16. Iso-surface of the flame front colored with the efficiency function showing the effect of increased modeled subgrid winkling. Snapshot of a representative cycle at -2 cad.

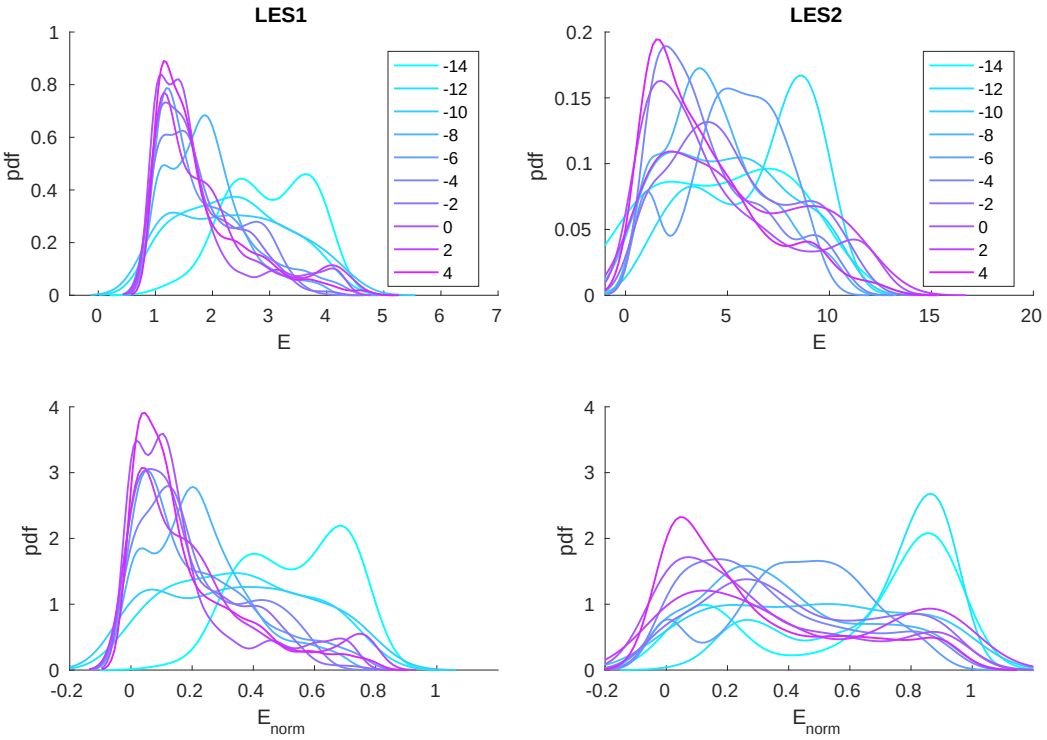

Figure 17. Probability distribution of the efficiency function extracted along the flame front for different cad. Top: $\mathcal{E}$; bottom: $(\mathcal{E}-1)/(\mathcal{E}_{\max}-1)$.

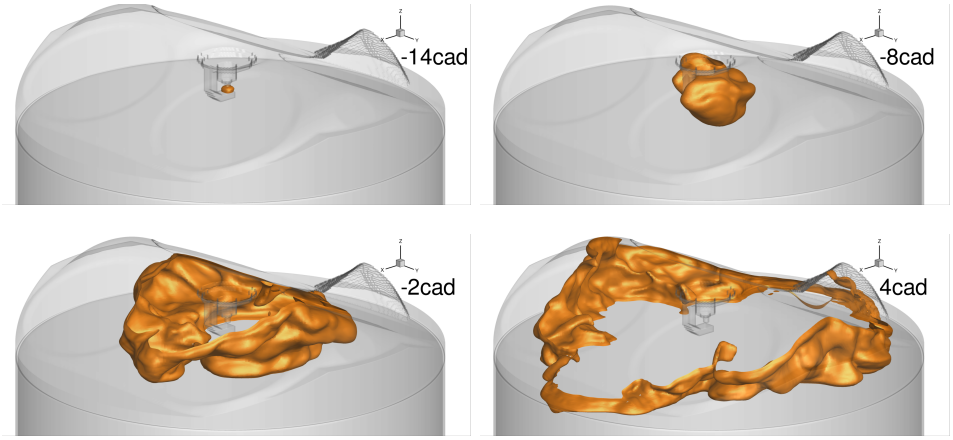

Figure 18. Turbulent flame propagation showing a single representative flame kernel expansion from *LES2*. The flame is visualized by an iso-surface of the progress variable (c=0.5) starting at 2 cad after ignition.

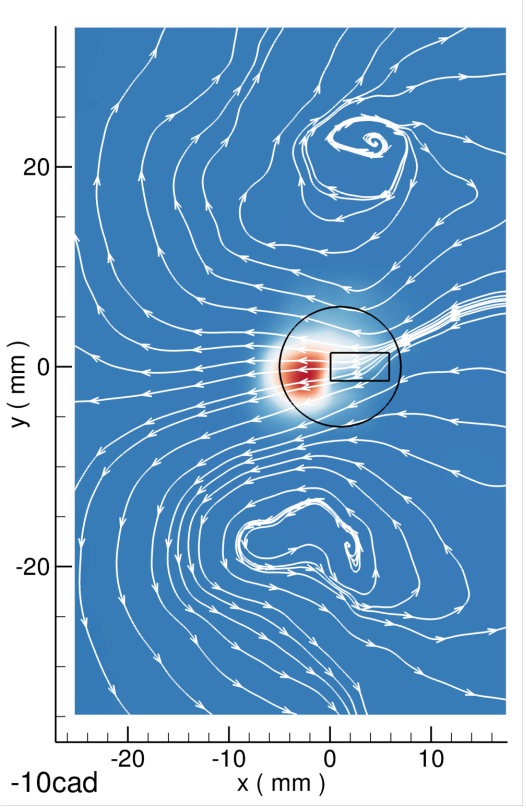

Figure 19. Averaged streamlines in the swirl plane superimposed onto the flame contour (progress variable showing the flame kernel in red) at an early stage after ignition (-10 cad). The spark plug being above the plane has been added for orientation (black).

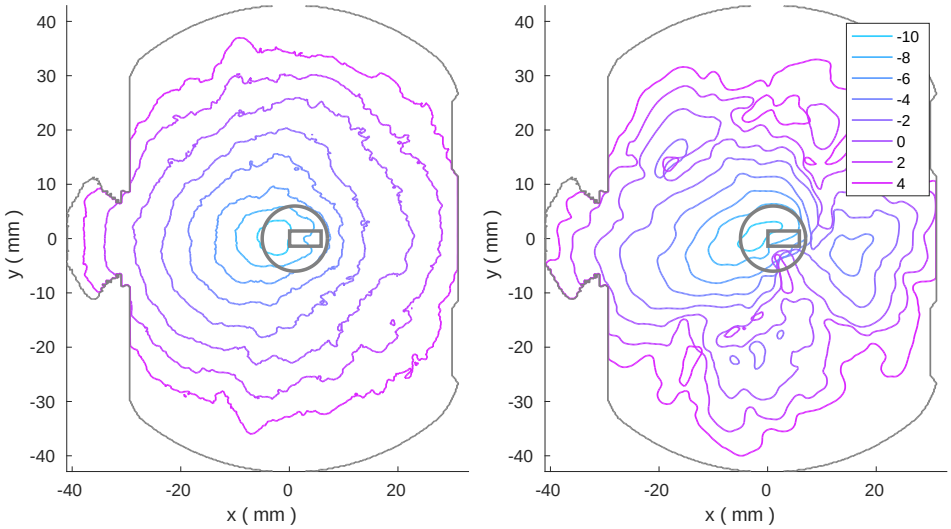

Figure 20. Flame contour in the swirl plane for several cad. Left: averaged; right: single cycle. The spark plug being above the plane has been added for orientation (gray).

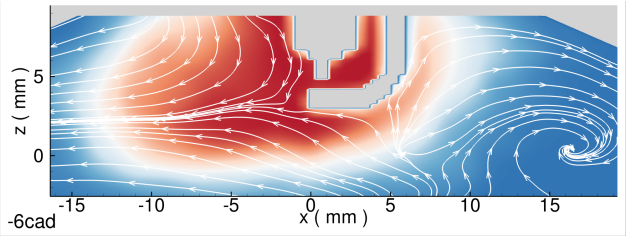

Figure 21. Averaged streamlines in the tumble plane superimposed onto the flame contour (progress variable showing the flame kernel in red) at an early stage after ignition (-6 cad).

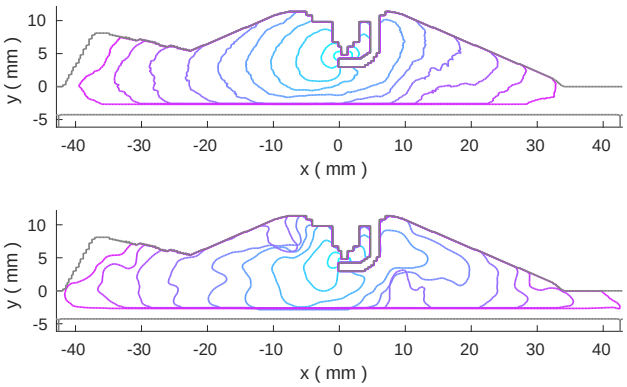

Figure 22. Flame contour in the tumble plane for several cad. Top: averaged; bottom: single cycle. Compared to Fig. 20 also contains smaller kernels (-14 cad and -12 cad) that did not yet reach the swirl plane.

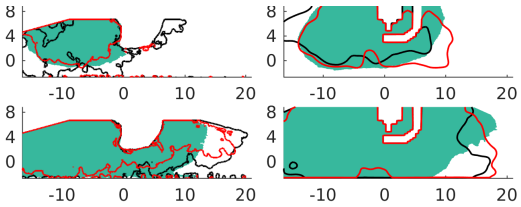

Figure 23. Illustration of the flame propagation in the tumble plane for cad=-6 (top) and cad=-2 (bottom). Flame position for two individual cycles (colored lines) and time averaged burnt gas region (green).Left: experiments, right: simulation.

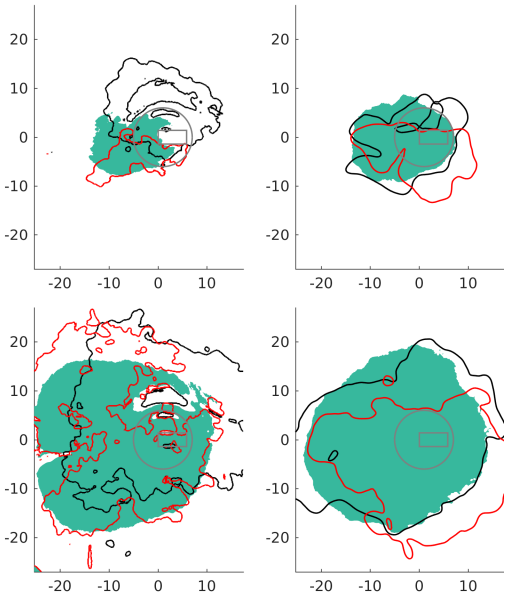

Figure 24. Illustration of the flame propagation in the swirl plane for cad=-6 (top) and cad=-2 (bottom). Flame position for two individual cycles (colored lines) and time averaged burnt gas region (green).Left: experiments, right: simulation.The spark plug being above the plane has been added for orientation (gray).

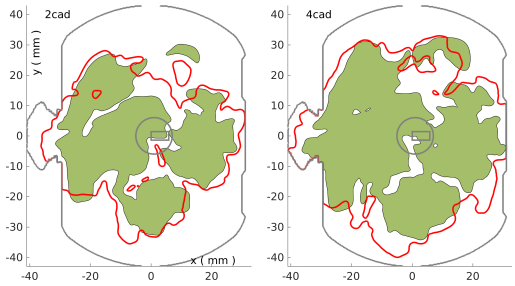

Figure 25. Comparison of the flame propagation within the swirl-plane as predicted by the *LES1* (filled area) and *LES2* (red curve). The spark plug being above the plane has been added for orientation (gray).

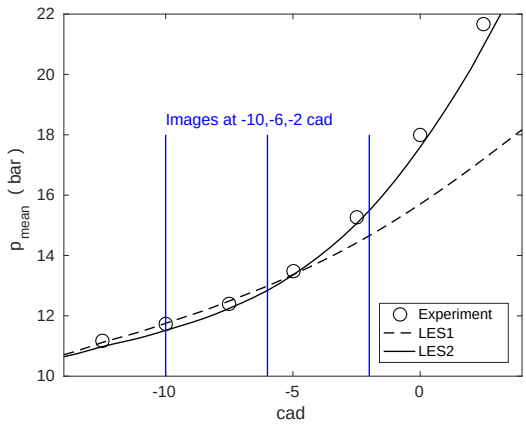

Figure 26. Magnified region of the pressure curve showing the section considered for the flame imaging.

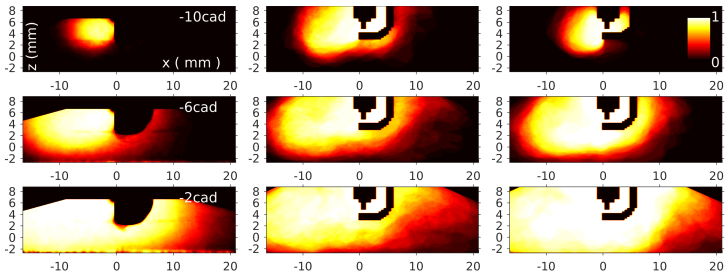

Figure 27. Averaged normalized reaction progress variable $\bar{c}$ within the tumble plane. Contour of the experiment (left), *LES1* (middle) and *LES2* (right).

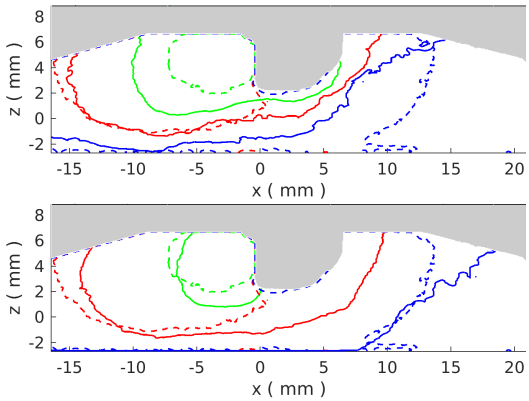

Figure 28. Iso-contour of $\bar{c} = 0.5$ for the corresponding cad at -10 (green), -6 (red) and -2 (blue) for the simulation (solid line) and the experiment (dashed line), respectively. *LES1* (top) and *LES2* (bottom).

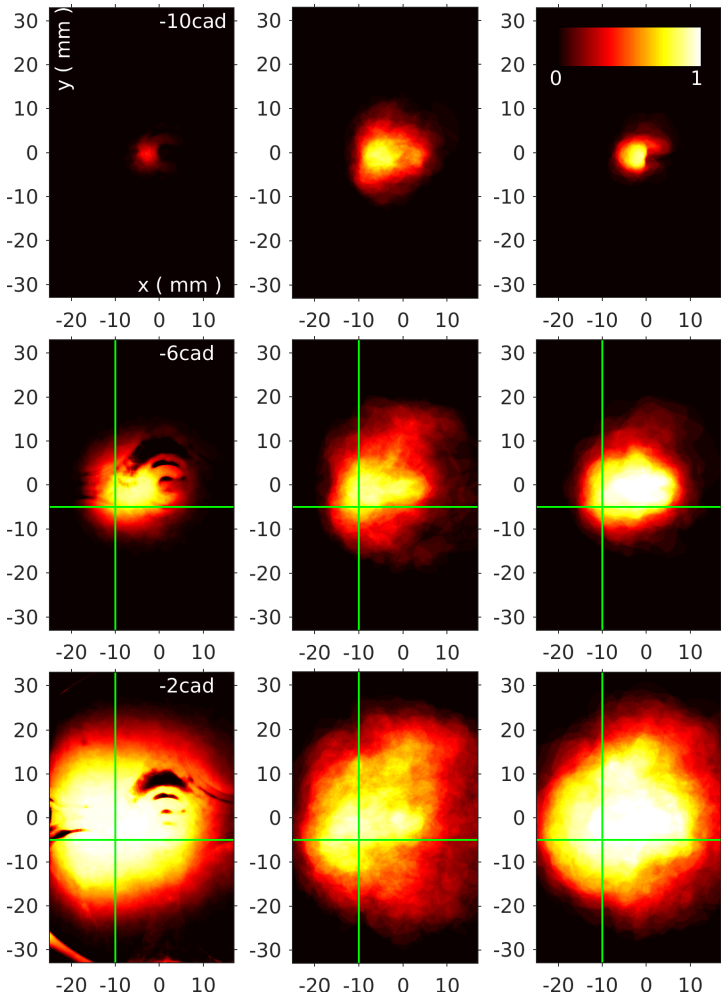

Figure 29. As in Fig. 27 but for the swirl plane being at z=1.3 mm. Holes in the measurements are due to reflections.

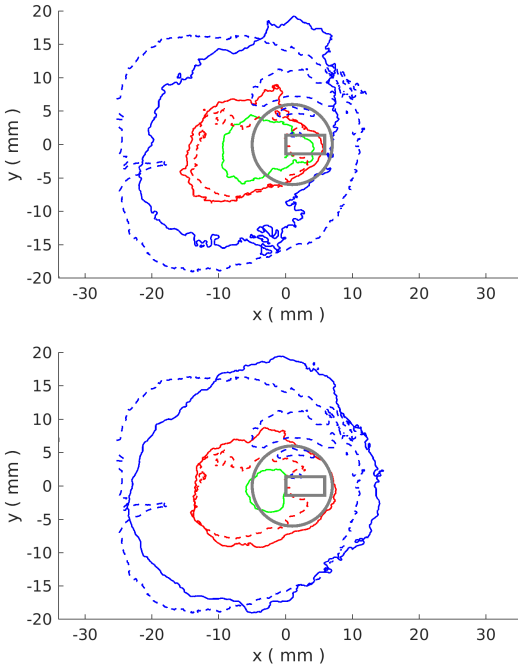

Figure 30. As in Fig. 28 but for the swirl plane being at z=1.3 mm. The spark plug being above the plane has been added for orientation (gray).

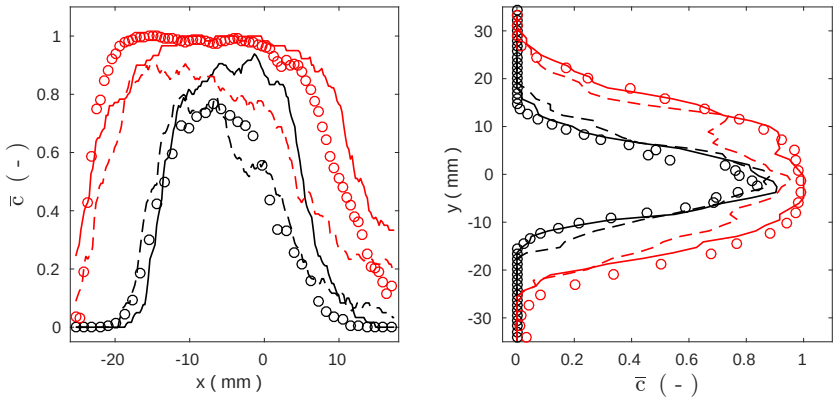

Figure 31. Averaged normalized reaction progress variable extracted along the lines as indicated in green in Fig. 29 for -6 (black) and -2 cad (red). The positions have been chosen to be outside reflections. Circle: experiment; dashed line: *LES1;* solid line: *LES2.*

List of Tables

Table 1. Engine operating conditions. Crank Angle Degrees (cad) are relative to Top-Dead-Center.

Compression ratio	8.5
Bore/Stroke	86/86 mm
Displacement volume	500 cm^2
Intake valve open/close	325/-125 cad
Exhaust valve open/close	105/-345 cad
Equivalence ratio / fuel	0.8/iso-octane
Rotational speed	800 rpm
Spark timing/dwell	-16 cad/3.5 ms
Mean P_{intake}/T_{intake}	950 mbar/49±2°C

Table 2. Parameters of the two simulations and summary of the predicted pressure.

	Experiment	*LES1*	*LES2*
Wrinkling factor	-	default ($\beta = 0.5, 1u'_\Delta$)	adjusted ($\beta = 0.8, 1.5u'_\Delta$)
Ignition kernel diameter	-	4 mm	1.5 mm
$p_{\max}$	29.27	23.28	29.59
$\mathrm{cad}(p_{\max})$	10	16	10
$p_{\mathrm{rms,max}}$	2.06	1.54	2.3
$\mathrm{cad}(p_{\mathrm{rms,max}})$	4.5	10	5